Mary Ann Liebert, Inc. - Image Cover Art

Notebook: Work
Created: 6/17/2012 11:31 AM
URL: http://online.liebertpub.com/action/showLargeCover?issue=40239833

Previous Issue

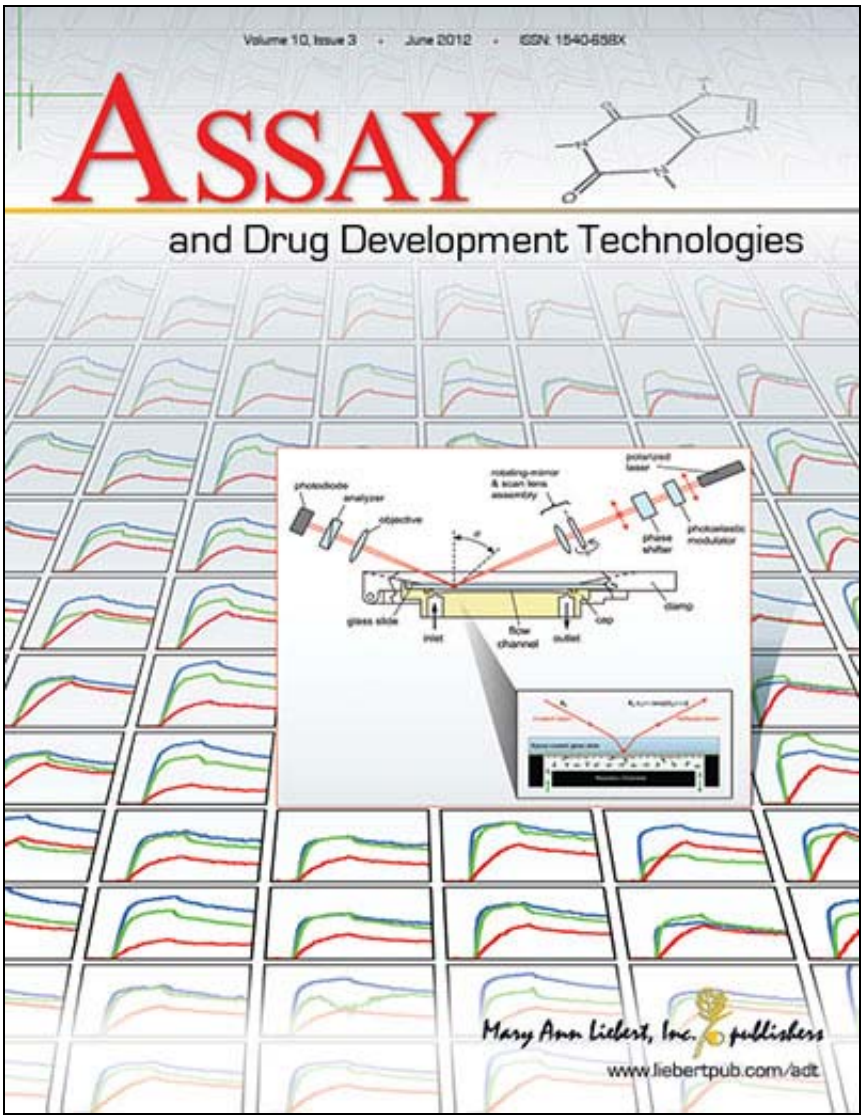

June 2012
Vol. 10, No. 3

Cover Caption: Advancing microarray technology from an endpoint assay to a kinetic constant assay platform. Molecular targets expressing a variety of epitopes are immobilized in the form of a large microarray on a chemically functionalized glass surface. ***Inset:*** By incubating the microarray in a solution of a probe that specifically recognizes some of the epitopes, the probes are then captured by the corresponding immobilized targets, causing the surface mass density of the target region to change. Such a change leads to *extra* change in

magnitude and phase (Δ*r* and Δδ) of an incident monochromatic light beam upon reflection from the surface. These changes are *label-free signatures of probe-target binding reactions*. A novel oblique-incidence reflectivity difference (OI-RD) scanning microscope (***foreground***) *directly* measures Δr and Δδ in real time and enables simultaneous detection of ~10,000 probe-target binding curves (***background***) in a single experiment. See “Simultaneous measurement of 10,000 protein–ligand affinity constants using microarray-based kinetic constant assays” by Landry *et al.*, this issue, p. 250. ***Upper right chemical structure:*** Theophylline. Cover design by Darryl Leja.

Simultaneous Measurement of 10,000 Protein-Ligand Affinity Constants Using Microarray-Based Kinetic Constant Assays

James P. Landry, Yiyan Fei, and Xiangdong Zhu

Department of Physics, University of California at Davis, Davis, California.

ABSTRACT

Fluorescence-based endpoint detection of microarrays with 10,000 or more molecular targets is a most useful tool for high-throughput profiling of biomolecular interactions, including screening large molecular libraries for novel protein ligands. However, endpoint fluorescence data such as images of reacted microarrays contain little information on kinetic rate constants, and the reliability of endpoint data as measures of binding affinity depends on reaction conditions and postreaction processing. We here report a simultaneous measurement of binding curves of a protein probe with 10,000 molecular targets in a microarray with an ellipsometry-based (label-free) optical scanner. The reaction rate constants extracted from these curves (k_{on}, k_{off}, and $k_a = k_{on}/k_{off}$) are used to characterize the probe-target interactions instead of the endpoints. This work advances the microarray technology to a new milestone, namely, from an endpoint assay to a kinetic constant assay platform. The throughput of this binding curve assay platform is comparable to those at the National Institutes of Health Molecular Library Screening Centers, making it a practical method in screening compound libraries for novel ligands and for system-wide affinity profiling of proteins, viruses, or whole cells against diverse molecular targets.

INTRODUCTION

Biomolecular microarrays have emerged as a leading high-throughput technology for system-wide biology such as genomics,[1–3] proteomics,[4–11] glycomics,[12–18] and small molecule drug discovery.[19–26] By immobilizing thousands or tens of thousands of molecular targets as distinct features on a solid support and simultaneously exposing all the targets to a probe solution of interest, chemical reactions of the probe with the targets are assayed at the same time. *In situ* synthesis is used to produce high-density peptide and oligonucleotide microarrays.[27] For majority of biomolecules including cDNA, proteins, carbohydrates, lipids, and small molecule compounds, contact-printing techniques are employed to fabricate target microarrays on chemically functionalized glass slides.[28,29] Printed microarrays easily have 10,000 to 35,000 features (or spots) over an area of 8 to 20 cm^2. The significance of these large target microarrays to system-level biology is obvious considering that the human genome has 25,000 protein-encoding genes,[30,31] the yeast proteome has 6000 proteins,[5,32] libraries of recombinantly expressed immunoglobulins (IgG) are typically of the order of 10,000 or smaller,[33,34] and libraries of small molecule compounds typically have 10^4–10^6 molecules.

So far, most microarrays are detected with fluorescence scanners, wherein solution-phase probe molecules are modified with a fluorescent label or an affinity tag before incubation with the microarray. After the incubation under specific conditions (*e.g.*, probe concentration, incubation time, temperature, and secondary reaction of affinity tags), the unbound probes are removed by washing before the "reacted" microarray is read with a fluorescence scanner. Such "endpoint" measurements do not provide information on reaction kinetic rate constants (the true measure of binding affinity) and the results may vary significantly when the target density on a microarray varies, a common occurrence for printed microarrays. Furthermore, depending upon the reaction rate constants, the reaction endpoints can vary as incubation conditions change. For example, relative affinity assessment based on endpoint fluorescence intensity often assumes that probe-target complexes increase linearly with time up to the end of incubation and that the complexes survive postreaction washing. Without the information on the association rate constants *a priori*, one needs to confirm experimentally the linear regime before the endpoint data can be so interpreted. In addition, without the information on dissociation rate constants, one cannot properly assess those probe-target complexes that do not survive post-incubation washing. The remedy to these drawbacks associated with endpoint assays is to observe binding reactions in real-time instead. In this case, one measures binding curves of the probe to immobilized targets during association and dissociation phases of reactions and extracts reaction rate constants from these curves as characterizing parameters of probe-target

ABBREVIATIONS: B-BSA, biotin-BSA; Dig, digoxin; DNP, 2,4-dinitrophenol; Glc, glucose; GT a-HM, polyclonal goat IgG against human IgG; GT a-MS, polyclonal goat IgG against mouse IgG; GT a-RB, polyclonal goat IgG against rabbit IgG; HM, human IgG; IB, iminobiotin; IgG, immunoglobulins; Mal, maltose; Metal, metallothionein; Meth, Methamphetamine; Morph, morphine; MS, mouse IgG; OI-RD, oblique-incidence reflectivity difference; PB, phenobarbital; PB-BSA, phenobarbital-BSA; PBS, phosphate buffered saline; RB, rabbit IgG; SPR, surface plasmon resonance; THC, tetrahydrocannabinol; THP, Theophylline.

DOI: 10.1089/adt.2011.0406

interactions. We will show as is expected that measurements of binding kinetic constants are independent of target density variation in a microarray. Furthermore from binding curves, one can assess other issues such as avidity, heterogeneity, mass transport, and conformational changes that are difficult to address by endpoint assays.

Fluorescence-based methods are seldom used for real-time binding curve measurements due to photobleaching suffered by many fluorescent tags and the potential effect of these tags on intrinsic association and dissociation rate constants.[35] Label-free optical biosensing methods, such as surface plasmon resonance reflectometry (SPR),[36–42] reflection interference spectroscopy,[43–45] dielectric wave guide reflectometry,[46–49] and imaging ellipsometry,[50–54] complement fluorescence-based detection by doing away with labeling and providing both endpoint and kinetic measurements of binding reactions. However, these biosensors only detect a small number of reactions (no more than a few hundred reactions) at a time and often require special (and costly) sensor surfaces. As a result, they are not suitable for large microarray detection with 10,000 or more immobilized targets.

In this report we demonstrate an ellipsometry-based optical sensor platform capable of simultaneous measurement of binding curves of a probe with 10,000 targets immobilized on a functionalized glass slide. This development advances microarray technology from an endpoint assay to a true binding affinity assay platform with a potential to assay over 50,000 targets in one day.

The summary of this detection platform is illustrated in *Fig. 1*. Molecular targets expressing specific epitopes are immobilized in form of a microarray on an epoxy-functionalized glass slide using a contact-printing robot. The unprinted surface is blocked with macromolecules that do not express the epitopes. By incubating the microarray in a solution of protein probes that specifically recognize the epitopes, the probes become captured by the immobilized targets, causing the thickness d or coverage Θ or generally the surface mass density Γ (gm/cm^2) of the immobilized target layer to change. The endpoint and/or real-time evolution of such a change lead to extra changes in magnitude and phase of an incident monochromatic light beam upon reflection from the glass surface. We directly measure the extra magnitude change Δr and extra phase change $\Delta\delta$ as fluorescenceless measures of the protein-target binding reactions.

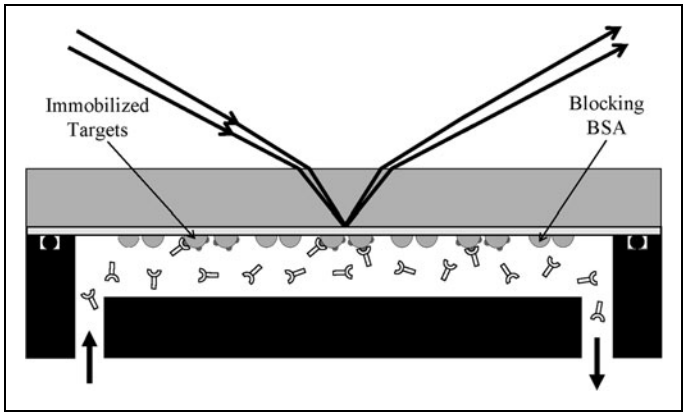

Fig. 1. Summary of a scanning ellipsometry-based detection of endpoints and real-time association–dissociation curves of protein probes with surface-immobilized targets in form of a large microarray on an epoxy-functionalized glass slide. The changes in thickness d and coverage Θ or surface mass density Γ of the target layer as a result of binding reaction cause extra changes in magnitude ($\Delta r = r - r_o$) and phase ($\Delta\delta = \delta - \delta_o$) of an incident light beam (E_o) upon reflection from the target-covered surface. r_o and δ_o are magnitude and phase changes due to reflection from the "bare" glass surface in the absence of the target-probe layer. The present ellipsometry-based detection platform measures Δr and $\Delta\delta$ in real-time from all immobilized targets.

METHODS AND MATERIALS

Oblique-Incidence Reflectivity Difference Scanning Microscope

Our optical sensor platform for large microarray detection is a scanning optical microscope based on polarization-modulated oblique-incidence reflectivity difference (OI-RD).[26,55–57] It does not require specially structured substrates such as gold films or dielectric waveguides for detection, and has a large "field of view" (presently $\sim 10\,\text{cm}^2$). It is thus fully compatible with large microarrays printed on inexpensively functionalized glass slides. Compared to imaging ellipsometers based on polarizer-compensator-sample-analyzer schemes,[50–54] the OI-RD scanning microscope is inherently more sensitive to surface-bound changes (*e.g.*, thickness and mass density) by more than one order of magnitude.[58]

The arrangement of our scanning OI-RD microscope used in this work is briefly described here (*Fig. 2*). A scan lens focuses a polarization-modulated He-Ne laser beam ($\lambda = 633$ nm) to a 30-μm-diameter spot on the back surface of a glass slide printed with a target microarray. The incidence angle is $\theta = 36.6°$ in the glass slide. The back surface is in contact with an aqueous solution in a fluidic chamber. Images of the microarray are obtained by raster scanning the beam across the back surface at a step size of 20 μm with a combination of a galvanometer mirror and the scan lens along the y-axis and by moving the microarray fluidic assembly relative to the beam along the x-axis with a linear stage. Image "contrast" is based upon the polarization change of the laser beam upon reflection from the back surface,[50,52] described by the ratio of reflection coefficients for p- and s-polarized components of the beam, $r_p/r_s = \tan\psi \cdot \exp(i\delta)$. An OI-RD scanning microscope directly measures the polarization change. When solution-phase probes bind to immobilized targets on the glass surface, the surface mass density (mass per unit area) of the target layer Γ changes and in turn alters r_p/r_s. When the target, the probe, and the glass slide are transparent at the optical wavelength λ, the change in Γ primarily alters the phase δ (see *Supplementary Data* for detailed description of $\Delta\delta$ measurement; Supplementary Data are available online at www.liebertonline.com/adt) as follows,[55,59,60]

$$\Delta\delta \cong \frac{-4\pi\sqrt{\varepsilon_s}\cos\theta}{(\varepsilon_0 - \varepsilon_s)(\cot^2\theta - \varepsilon_s/\varepsilon_0)} \cdot \frac{(\varepsilon_d - \varepsilon_0)(\varepsilon_d - \varepsilon_s)}{\varepsilon_d}\left(\frac{\Gamma}{\rho\lambda}\right). \quad (1)$$

ε_s, ε_0, and ε_d are the optical dielectric constants of the glass slide, the aqueous solution, and the probe-target layer, respectively. $\rho = 1.35$ g/

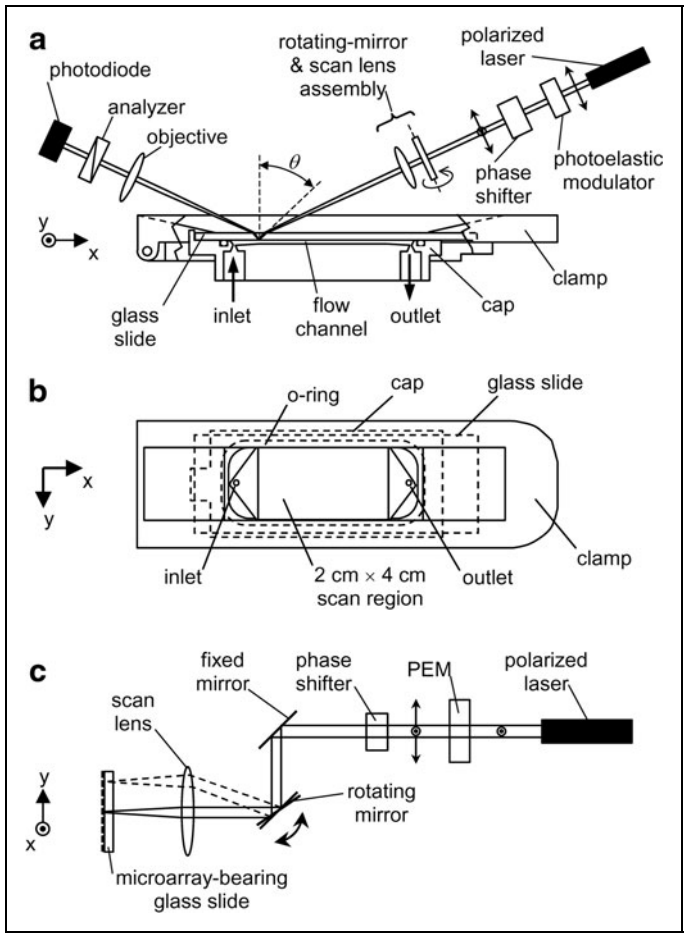

Fig. 2. **(a)** Optical layout of the scanning OI-RD microscope. A functionalized glass slide with a microarray printed on the bottom surface is installed in a fluidic chamber assembly. An illumination laser beam is raster swept across the microarray with a scan mirror assembly for *y*-scan; a linear translation stage moves the fluidic chamber assembly with respect to the illumination optics in the orthogonal direction for *x*-scan. **(b)** The fluidic chamber assembly showing the 2 cm × 4 cm accessible area of the glass slide. **(c)** Side view of the microscope illustrating the *y*-scan. OI-RD, oblique-incidence reflectivity difference.

cm^3 is the volume mass density of globular proteins.[61] With typical values of $\varepsilon_s = 2.31$, $\varepsilon_0 = 1.77$, and $\varepsilon_d = 2.03$, a probe-target layer with $\Gamma = 1\ ng/mm^2$ yields $\Delta\delta = -2.3 \times 10^{-3}$. The current limit of our OI-RD microscope is $|\Delta\delta| \sim 2 \times 10^{-5}$, corresponding to a surface mass density of protein probes in the order of $\sim 10\ pg/mm^2$. It is not yet as sensitive as surface-plasmon-resonance or waveguide-based sensors since we have not yet utilized the resonance-like enhancement factor $1/(\cot^2\theta - \varepsilon_s/\varepsilon_0)$ in Equation (1). However, the high throughput and low operation cost of the OI-RD scanning microscope for compound screening are the major merits when compared to these other label-free detection methodologies.

For simultaneous measurement of binding curves of a probe to thousands of immobilized targets, we perform repeated scans of a subset of pixels on the microarray surface as follows. We select one pixel from each target spot as the signal channel and two pixels from the unprinted region on two sides of the target as the reference channels. Each reference channel is shared by two neighboring signal channels. The signal and reference pixels along vertical and horizontal lines form a rectangular readout grid. For a 9216 (64 × 144) spot microarray, the readout grid has 9216 target channels and 9,360 reference channels. We scan these channels in every 20–70 s. The optical signal $\Delta\delta$ from a signal channel minus the averaged optical signal from the two neighboring reference channels yields the background-corrected signal for the target. This procedure compensates for instrumental drift, ambient refractive index changes, and flow-induced signal transients. The time series of the background-corrected signal from a target collected during the course of a reaction form a binding curve of the probe against the target.

Microarray Targets and Probes

Targets. Bovine serum albumin (BSA), human IgG (HM), mouse IgG (MS), rabbit IgG (RB), and polyclonal goat IgG against human/mouse/RB (GT anti-HM, GT anti-MS, and GT anti-RB) were purchased from Jackson ImmunoResearch Laboratories. Methamphetamine-BSA, tetrahydrocannabinol-BSA, and morphine-BSA conjugates were purchased from Biodesign International. Theophylline-BSA, phenobarbital-BSA (PB-BSA), and digoxin-BSA were purchased from Fitzgerald Industries International, Inc. Metallothionein (Metal) and biotin-*N*-hydroxysuccinimidyl ester (NHS-biotin ester) were purchased from Sigma-Aldrich.

We prepared biotin-BSA (B-BSA) conjugates by reacting NHS-biotin ester with a BSA solution in 0.1 M $NaHCO_3$. The loading of biotin was controlled by the molar ratio of the NHS-biotin ester to BSA that ranged from 5×, 10×, 20×, up to 40×. Excess free biotin was removed by dialysis. We prepared iminobiotin-BSA conjugates similarly. We made 2,4-dinitrophenol-BSA conjugates with a previously described method.[25] We also made glucose-BSA and maltose-BSA by reductive amination at pH 8.0.[62]

Probes. Monoclonal mouse anti-biotin IgG was purchased from Jackson ImmunoResearch. Monoclonal mouse anti-methamphetamine, anti-tetrahydrocannabinol, anti-phenobarbital, and anti-theophylline IgG were purchased from Biodesign. Monoclonal mouse anti-morphine IgG was purchased from Fitzgerald Industries. Polyclonal goat anti-2,4-dinitrophenol was purchased from Sigma-Aldrich. Concanavalin A was purchased from Vector Laboratories.

Microarray Fabrication and Reaction

Microarrays of 9216 (64 × 144) or 10,880 (68 × 160) targets were printed on epoxy-functionalized glass slides (ArrayIt Corporation) using an OmniGrid 100 contact-printing robot (Digilab). Each microarray covers a 2 cm × 4 cm area. A printed microarray without further processing was installed in a fluidic chamber assembly (*Fig. 2*) and imaged with the OI-RD scanner before exposed to a buffer solution. The large optical signals from printed materials including

the buffer salts were used (i) to align the microarray axes to the scan axes and (ii) to generate a rectangular readout grid for real-time binding curve measurement and image analysis (see *Supplementary Data* for details). It takes 18 min to acquire an OI-RD image of an 8-cm^2 area with a pixel size (scan step size) of 20 μm × 20 μm. The microarray was then washed *in situ* by passing several milliliters of 1 × phosphate buffered saline (PBS) buffer through the fluidic chamber and imaged again for a record of the target density. Next, the washed microarray was exposed to a solution of 7.6 μM BSA (0.5 mg/mL) in 1 × PBS for 30 min to quench unreacted epoxide groups to prevent nonspecific binding of subsequent probes to the unprinted surface. After BSA blocking, the microarray was kept in 1 × PBS and ready for binding reactions.

All binding reactions were performed at ambient temperature (nominally 25°C). For each reaction, we first passed 1 × PBS buffer through the fluidic chamber at 0.01 mL/min for 30 min to acquire the baseline. Next, the buffer was quickly replaced with a probe solution at 5 mL/min for 12 s. The flow rate of the solution was then reduced to 0.01 mL/min to allow the probe to react with the microarray at a constant concentration for 30–60 min (association phase of the reaction). Afterward, the probe solution was quickly replaced with 1 × PBS buffer at 5 mL/min for 12 s. The flow rate of the buffer was subsequently reduced to 0.01 mL/min to allow the captured probe to dissociate from the microarray for 60 or 90 min (dissociation phase of the reaction). We acquired OI-RD images of the microarray before and after the reaction. During the reaction, we repeatedly scanned the readout grid every 20–70 s to acquire binding curves from all targets. We note that if the association and/or dissociation for some of the reactions take minutes or less to finish, the association–dissociation curves of these reactions (much fewer than 10,000) can be revisited on a separate but same microarray in a "cherry-picking" mode with a time step as short as a few seconds, limited only by how quick the buffer is replaced by the probe solutions and vise versa.

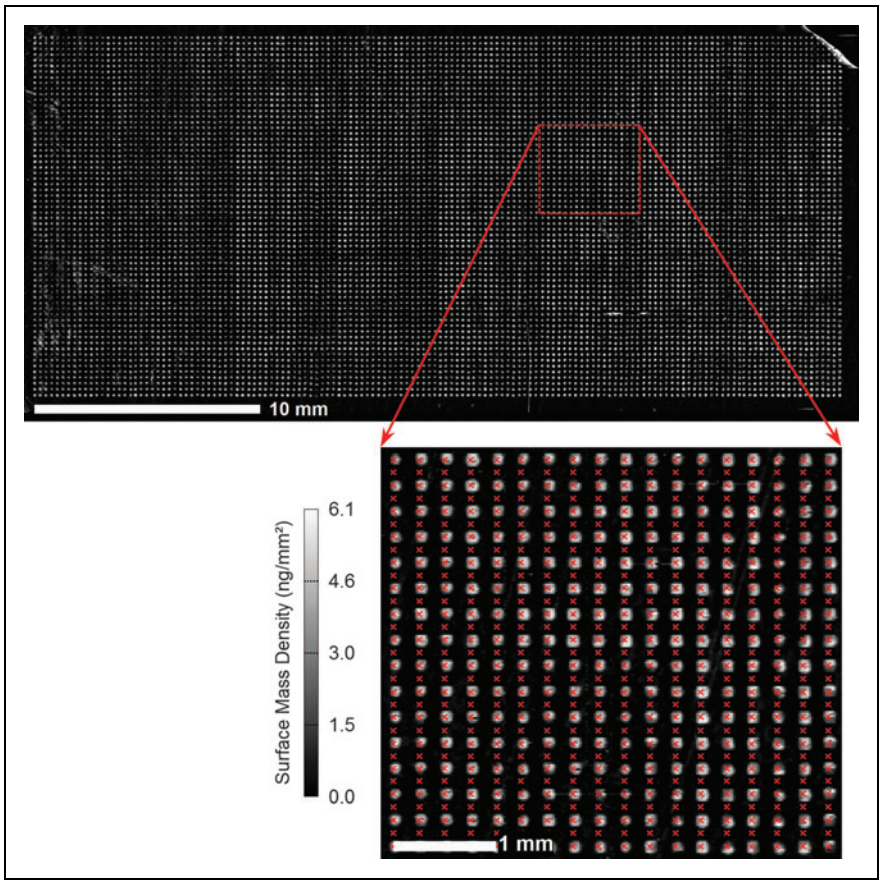

Fig. 3. OI-RD image of a biotinylated BSA microarray (64 × 144 spots) acquired after the microarray is washed with 1 × PBS buffer. The image pixel size is 20 μm and the center-to-center spacing of the spots is 250 μm. The inset is a magnified view that displays the discrete readout points (red crosses) used during real-time experiments. PBS, phosphate buffered saline.

RESULTS AND ANALYSIS

Binding Curves of a Protein Probe to a Microarray with 9216 Identical Targets

To demonstrate simultaneous detection of ~10,000 binding curves with the OI-RD scanning microscope, we performed the reaction of mouse anti-biotin IgG with a microarray with 9216 identical B-BSA targets. The targets were printed from a B-BSA solution at 1.6 μM in 1 × PBS. *Figure 3* shows the OI-RD image of the microarray in 1 × PBS after excess printed material was washed off. The surface mass density of the target layer averaged over the

Fig. 4. **(a)** 288 out of 9,216 simultaneously acquired OI-RD measurements of anti-biotin IgG (33 nM) binding to biotinylated-BSA microarrays. After a 30-min baseline measurement, the association reaction was monitored for 60 min (probe solution flowed starting at $t = 0$ min) and the dissociation reaction was monitored for 90 min (buffer solution flowed starting at $t = 60$ min). **(b)** Anti-biotin IgG binding curve sets (33 nM, 100 nM, and 300 nM) were acquired separately with fresh microarrays. For global curve fitting analysis of the data, binding curves from corresponding spot locations in each dataset are collected together as shown here (red curves = 33 nM, green curves = 100 nM, blue curves = 300 nM).

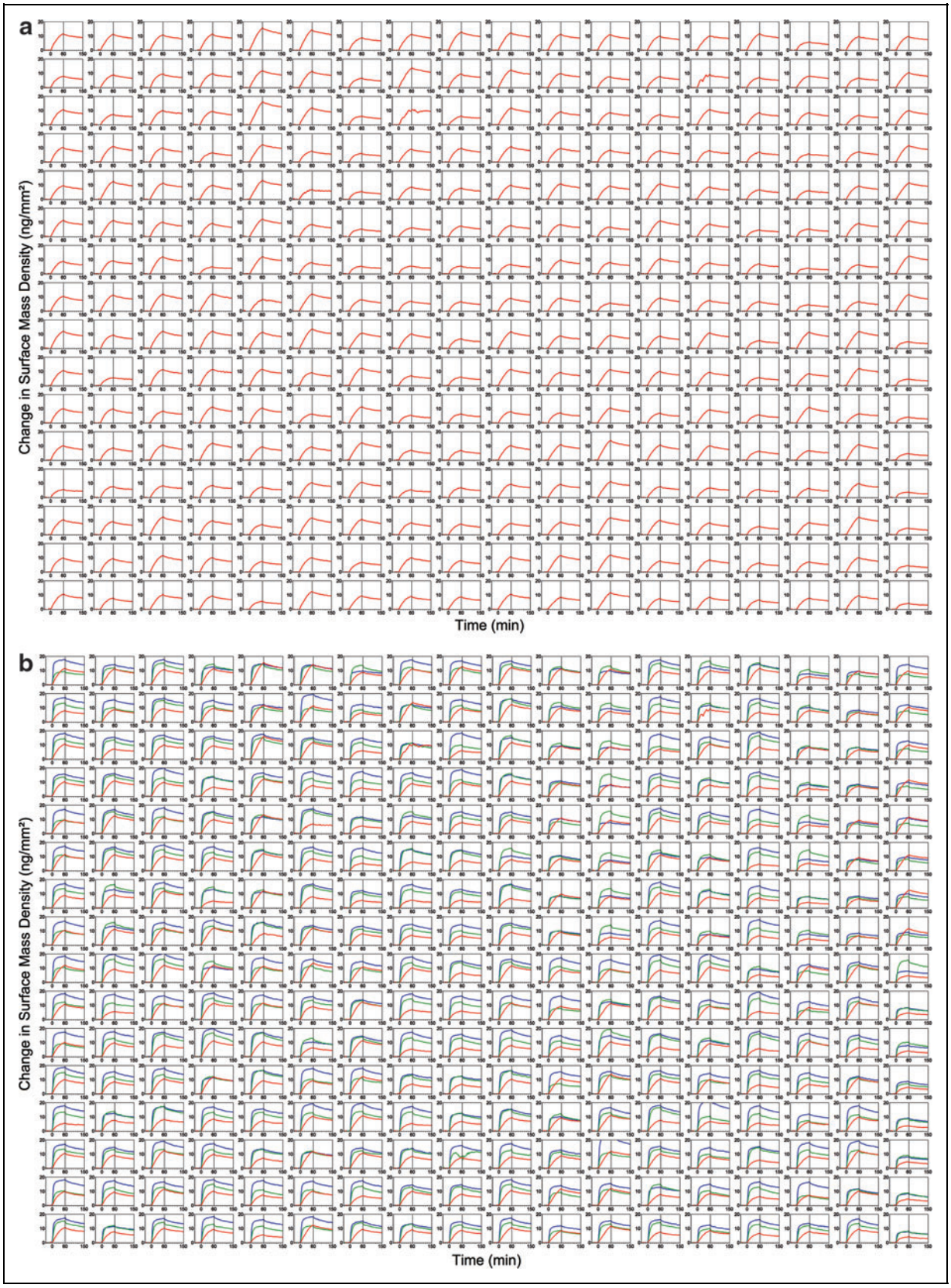
a
Change in Surface Mass Density (ng/mm²)
Time (min)
b
Change in Surface Mass Density (ng/mm²)
Time (min)

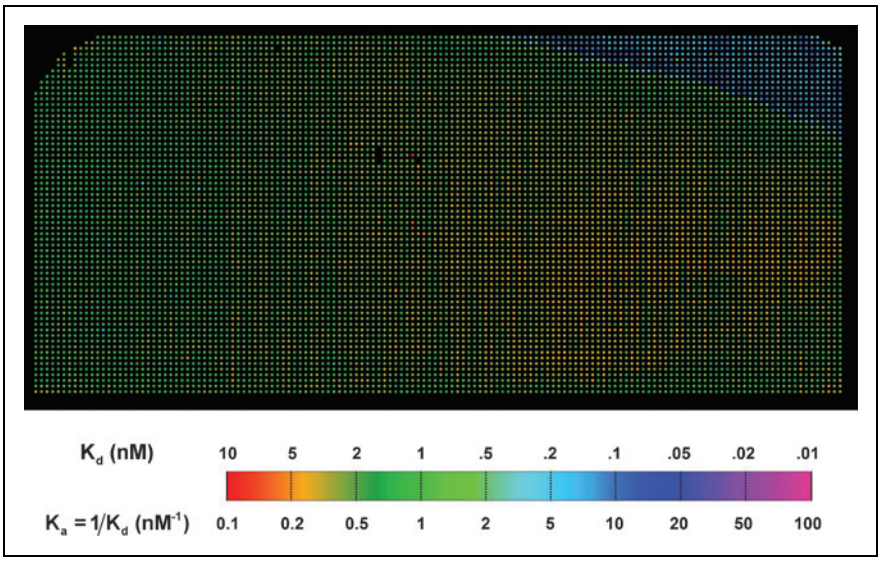

Fig. 5. Experimental equilibrium association constants K_a of mouse IgG (MS) anti-biotin probe binding to 9216 B-BSA targets, displayed in the same layout as the target microarray (*Fig. 3*). The equilibrium association constant at each microarray address is determined by $K_a = k_{on}/k_{off}$, where k_{on} and k_{off} are the global fitting parameters determined from the corresponding binding curve set (*Fig. 4*). IgG, immunoglobulins.

spot is 3.0 ± 0.5 ng/mm^2, corresponding to a full monolayer of B-BSA (a side-on oriented BSA monolayer has a surface mass density[56] of ~ 2 ng/mm^2). The variation within a spot is ± 1.3 ng/mm^2. *Figure 4a* displays 288 of 9216 simultaneously acquired binding curves at the MS concentration of $C = 33$ nM in $1 \times$PBS. Each curve records the change in OI-RD signal and in turn, through Equation (1), the change in surface mass density of the probe-target layer. The average surface mass density of captured IgG molecules at saturation is 5 ng/mm^2, so that on average every two immobilized B-BSA molecules captured one IgG molecule. This is the first report where binding curves were recorded for $\sim$10,000 features in a microarray in a single measurement. By repeating the binding curve measurement at the MS concentrations of $C = 100$ nM and 300 nM in two separate measurements, we obtained 9216 sets of binding curves, each set corresponding to the probe reaction with a distinct target at three probe concentrations. *Figure 4b* displays 288 of 9216 binding curve sets.

The 9216 binding curve sets were analyzed to yield the reaction kinetic rate constants using the Langmuir reaction model. In this model solution-phase probes are assumed to bind to surface-immobilized targets at a rate proportional to the probe concentration C, $k_{on}C$. The captured probes can dissociate from probe-target complexes at a rate k_{off}, independent of C. When the probe solution is introduced to the microarray at $t = 0$ and then replaced with $1 \times$PBS at a later time $t = t_0$, the number of captured probes per unit target area is

$$N(t) = N_0 \cdot \frac{k_{on}C}{k_{on}C + k_{off}} \left(1 - e^{-(k_{on}C + k_{off})t}\right) \quad (2a)$$

for $t < t_0$ and

$$N(t) = N_0 \cdot \frac{k_{on}C}{k_{on}C + k_{off}} (1 - e^{-(k_{on}C + k_{off})t_0}) e^{-k_{off}(t - t_0)} \quad (2b)$$

for $t > t_0$. N_0 is the maximum number of probes that can be captured per unit target area. It depends on factors such as the target density, geometric shapes and orientations of targets and probes. The surface mass density Γ in Equation (1) is proportional to $N(t)$ and as a result $\Delta\delta(t) = \gamma \times N(t)$. γ is a function of optical parameters displayed in Equation (1), and the volume mass density and molecular weight of the probe. We extract reaction rate constants k_{on} and k_{off} by fitting binding curve sets to Equations (2a) and (2b) simultaneously. Generally, N_0 varies from spot to spot in a microarray and from microarray to microarray due to variation in wetting properties across a functionalized glass surface and in the liquid delivery of contact printing. As a result, we treat N_0 as a fitting parameter that may vary from curve to curve within a set while treating k_{on} and k_{off} as common (global) parameters to all three curves of the set.[63–65] Details are described in *Supplementary Data*.

We computed the equilibrium association constants $K_a = k_{on}/k_{off}$ from the fitting parameters k_{on} and k_{off} for all 9,216 reactions. In *Figure 5*, we display K_a of mouse anti-biotin IgG reaction with 9216 B-BSA targets in the same layout as the target microarray (*Fig. 3*). This is the first equilibrium association constant map obtained from simultaneous measurement of 9216 binding curves on a microarray platform. Except for the upper-right corner of the microarray where the binding curves showed little dissociation (due to the insufficient buffer flow from left to right during the dissociation phase), the equilibrium association constants have a mean of 0.43 nM^{-1} and a standard error of ± 0.13 nM^{-1}, or $K_d = 1/K_a = 2.3$ nM $\pm$ 0.7 nM. Since the targets are of the same material, the standard error represents the uncertainty if a single B-BSA spot in a microarray is used to measure the equilibrium association constant to the probe. Given the inherent variations in contact-printed microarrays as described previously, the precision of this high-throughput kinetic constant assay is remarkably satisfactory. The slight decrease in K_a in *Figure 5* from left to right is presumably the result of the depletion effect. The result can be used to quantify the depletion effect along the length of the sample chamber.

Binding Curves of Multiple Probes to a 10,880-spot Microarray with Different Targets Printed Over a Range of Concentrations

We applied this binding kinetic constant assay to a 10,880-spot microarray with a diversity of 24 target types, each printed in concentrations ranging from 0.5 μM to 16 μM so that the target density

changes intentionally by a factor of 20. *Figure 6* shows the OI-RD image of such a microarray in 1×PBS after excess printed materials were washed off. The microarray consists of 16 identical subarrays, with the 24 targets in each subarray laid out as shown in the inset of *Figure 6*. Each target was printed in quadruplicate and at six printing concentrations, changing two-fold from 16 μM to 0.5 μM. The targets include (i) B-BSA with different amounts of conjugated biotin, (ii) carbohydrate-BSA conjugates (glucose and maltose), (iii) drug-BSA conjugates, and (iv) whole IgG molecules. Border columns and rows were printed with BSA at 1.6 μM as controls. The real-time readout grid consisted of a total of 10,240 target channels (some BSA rows were skipped) and 10,880 reference channels, and was raster scanned every 22 s to obtain 10,240 binding curves.

The microarray was reacted sequentially with multiple protein probes. They were, in order of reaction, anti-phenobarbital IgG, concanavalin A (lectin), anti-theophylline IgG, anti-biotin IgG, anti-tetrahydrocannabinol IgG, anti-morphine IgG, anti-dinitrophenol IgG, and anti-methamphetamine IgG. The reaction sequence was repeated on separate fresh microarrays to obtain binding curve sets for four probe concentrations of 300 nM, 100 nM, 33 nM, and 11 nM. The binding curve measurement consisted of a 30-min baseline in 1×PBS, a 30-min association phase in a probe solution, and a 60-min dissociation phase in 1×PBS under the same flow conditions as described previously.

In *Figure 7*, we show the K_a map of anti-biotin IgG reactions with 10,880 targets. In *Figure 8*, we show the K_a map of anti-phenobarbital IgG reactions with the same 10,880 targets. Zooming in on one subarray, we note that except for targets printed at the highest concentration of 16 μM (see Sun *et al.*,[25] who reported that at high printing concentrations and thus high immobilized target densities, the association rate of a solution-phase protein probe to the surface-bound targets deviates considerably from the rate obtained at lower printing concentrations, partly due to stereo-hindrance effect), $K_a = 0.53$ nM^{-1} of anti-biotin IgG to immobilized B-BSA is essentially the same even when both the target density and the amount of captured IgG molecules vary by a factor of 10–20. The magnitude is very close to the bulk value of 0.59 nM^{-1} reported by Jung *et al.*[66] and is 2.5 times the value reported by Adamczyk *et al.* in an SPR measurement.[67] The K_a of anti-phenobarbital IgG to immobilized PB-BSA is similarly independent of the target density, and its value of 2.7 nM^{-1} compares well with the affinity constant of ~20 nM^{-1} for monoclonal mouse anti-drug IgG molecules available from Fitzgerald Industries International, Inc. (www.fitzgerald-fii.com/Products?pId9&tsId = 21). This validates the notion that reaction rate constants obtained from global fitting

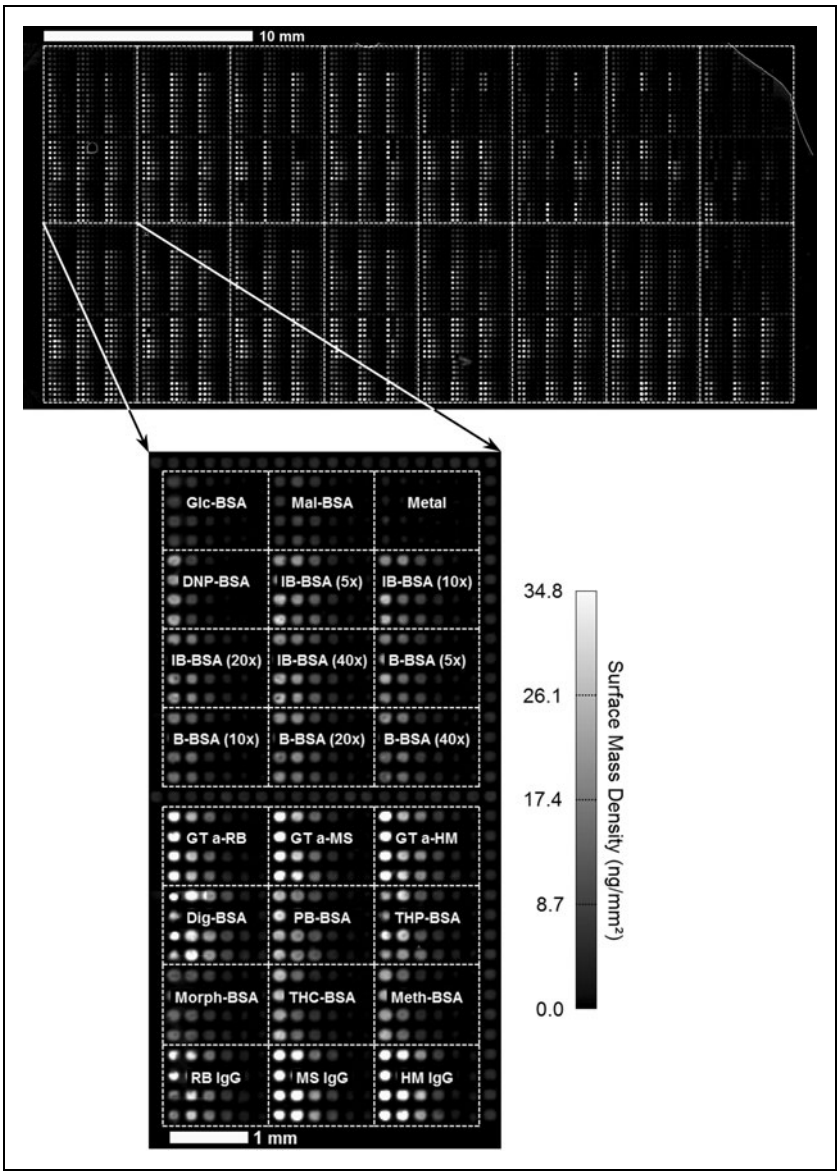

Fig. 6. OI-RD image of a ligand microarray (68×160 spots) acquired after washing the microarray with 1×PBS buffer, but before further reaction of the microarray. The image pixel size is 20 μm and the center-to-center spacing of the spots is 250 μm vertically and 225 μm horizontally. The red lines in the top panel show the outlines of 16 identical subarrays and the inset shows the detailed spot layout of each. Each target type was printed in quadruplicate in six different printing concentrations ranging from 16 μM (left) to 0.5 μM (right). BSA borders and unprinted spots are also included as controls. B-BSA, biotin-BSA; Dig, digoxin; DNP, 2,4-dinitrophenol; Glc, glucose; GT a-HM, polyclonal goat IgG against human IgG; GT a-MS, polyclonal goat IgG against MS; GT a-RB, polyclonal goat IgG against rabbit IgG; HM, human IgG; IB, iminobiotin; Mal, maltose; Metal, metallothionein; Meth, Methamphetamine; Morph, morphine; PB, phenobarbital; RB, rabbit IgG; THC, tetrahydrocannabinol; THP, Theophylline.

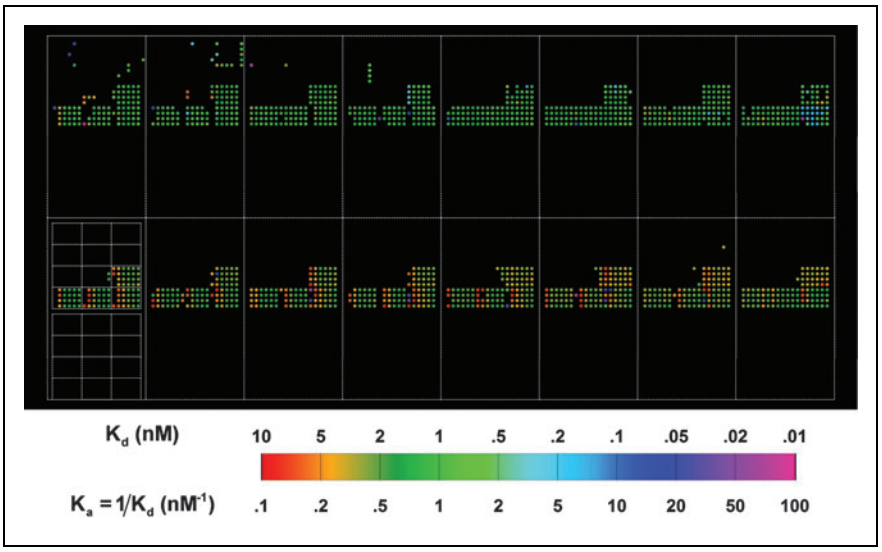

Fig. 7. Experimental equilibrium association constants K_a of MS anti-biotin probe binding to 10,880 targets, displayed in the same layout as the target microarray (*Fig. 6*). The white lines show the outlines of the 16 identical subarrays and the 4×6 blocks of spots printed with different concentrations of a particular target type.

binding curves are not and should not subject to ubiquitous target density variation in a contact-printed microarray and is independent of which pixel within a printed spot is used for binding curve measurement. It confirms that our present microarray-based kinetic constant assay is a robust platform for characterizing protein-ligand affinity. Similar findings for the other protein probes are described in *Supplementary Data*.

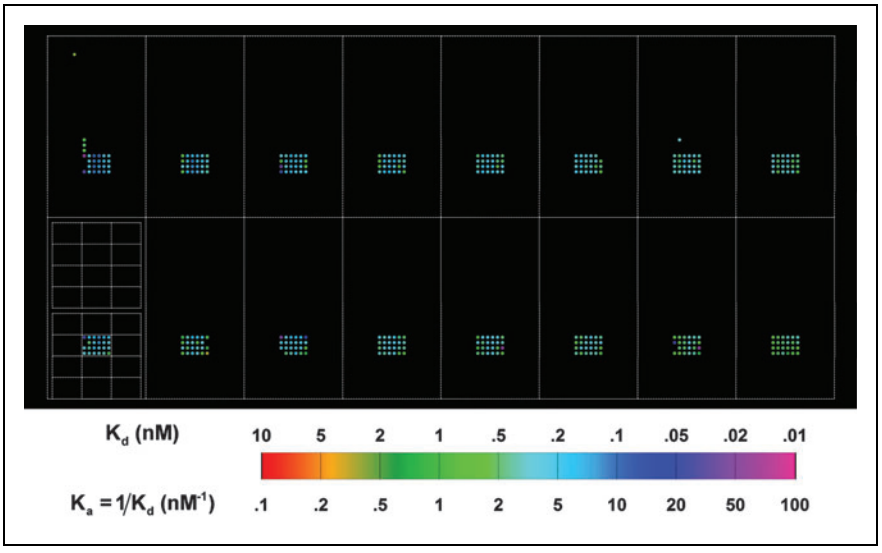

Fig. 8. Experimental equilibrium association constants K_a of MS anti-phenobarbital probe binding to 10,880 targets, displayed in the same layout as the target microarray (*Fig. 6*). The white lines show the outlines of the 16 identical subarrays and the 4×6 blocks of spots printed with different concentrations of a particular target type.

DISCUSSION AND CONCLUSION

Microarray-based binding assays have so far been successfully applied to parallel studies of multiple biomolecular interactions,[10,17,68] particularly to screening molecular libraries for protein ligands of interest.[5,11,18,23,24] This platform will profit enormously from real-time binding curve detection capability that directly yields reaction rate constants (intrinsic characteristics of biomolecular interactions) with essentially the same throughput. Since extraction of kinetic rate constants from binding curve sets is insensitive to the immobilization target density, binding curve assays solve the problem of target density variation that often plagues microarray-based endpoint assays. As a bonus, OI-RD images of a target microarray acquired before and after BSA blocking in fact provide a label-free measure of the target density.[56] Furthermore, binding curve assays detect those probe-target reactions with high dissociation rates that are easily missed in endpoint assays as a result of post-incubation washing. Though not elaborated here, real-time binding curves reveal other concurrent or sequential processes such as dissociation or conformational change of targets and the presence of multiple configurations of probe-target complexes (due to multiple binding pockets on a probe or multiple binding site presentation of the immobilized target) that are essentially beyond the reach of endpoint assays.

As to whether the present binding constant assay platform has the suitable throughput for large-scale molecular library screening, we observe that with one OI-RD scanning microscope, we can obtain binding curves of one protein probe to 50,000 targets (immobilized as 4 microarrays) at one concentration in one day. With three such OI-RD scanning microscopes, we can obtain 50,000 sets of binding curves at three probe concentrations to yield K_a of the probe to the 50,000 targets in a day. This means that we should be able to measure the equilibrium association constants of a single probe to 250,000 molecular targets in one week. This promises a new era for massive parallel characterization of biomolecular interactions.

We recently immobilized 8,000 drug-like small molecules (from NCI/DTP) on isocyanate-functionalized glass slide surfaces and screened these compounds for ligands of vascular endothelial growth factor (VEGF) with inhibitory effect against VEGF-KDR binding reaction using this

microscope. The result demonstrated that the method described in this article would work equally well for drug-like compounds as surface immobilized targets.

ACKNOWLEDGMENTS

This work was supported by the National Institutes of Health under R01-HG003827 and by the University of California under UC Discovery Grant #bio09-156225.

DISCLOSURE STATEMENT

No competing financial interests exist.

REFERENCES

1. Schena M, Shalon D, Davis RW, Brown PO: Quantitative monitoring of gene expression patterns with a complementary DNA microarray. *Science* 1995; 270:467–470.
2. "The chipping forecast." *Nat Genet* 1999;21(1 Suppl):1–60.
3. "The chipping forecast II." *Nat Genet* 2002;32(4 Suppl):461–552.
4. MacBeath G, Schreiber SL: Printing proteins as microarrays for high-throughput function determination. *Science* 2000;289:1760–1763.
5. Zhu H, Bilgin M, Bangham R, *et al.*: Global analysis of protein activities using proteome chips. *Science* 2001;293:2101–2105.
6. Haab BB, Dunham MJ, Brown PO: Protein microarrays for highly parallel detection and quantification of specific proteins and antibodies in complex solutions. *Genome Biol* 2001;2:1–13.
7. Espejo A, Cote J, Bednarek A, Richard S, Bedford MT: A protein-domain microarray identifies novel protein-protein interactions. *Biochem J* 2002;367: 697–702.
8. Miller JC, Zhou H, Kwekel J, *et al.*: Antibody microarray profiling of human prostate cancer sera: Antibody screening and identification of potential biomarkers. *Proteomics* 2003;3:56–63.
9. Nielsen UB, Cardone MH, Sinskey AJ, MacBeath G, Sorger PK: Profiling receptor tyrosine kinase activation by using Ab microarrays. *Proc Natl Acad Sci U S A* 2003;100:9330–9335.
10. Jones RB, Gordus A, Krall JA, MacBeath G: A quantitative protein interaction network for the ErbB receptors using protein microarrays. *Nature* 2006;439: 168–174.
11. Michaud GA, Salcius M, Zhou F, *et al.*: Analyzing antibody specificity with whole proteome microarrays. *Nat Biotechnol* 2003;21,1509–1512.
12. Wang D, Liu S, Trummer BJ, Deng C, Wang A: Carbohydrate microarrays for the recognition of cross-reactive molecular markers of microbes and host cells. *Nat Biotechnol* 2002;20,275–281.
13. Blixt O, Head S, Mondala T, *et al.*: Printed covalent glycan array for ligand profiling of diverse glycan binding proteins. *Proc Natl Acad Sci U S A* 2004;101:17033–17038.
14. Lee M, Shin I: Facile preparation of carbohydrate microarrays by site-specific, covalent immobilization of unmodified carbohydrates on hydrazide-coated glass slides. *Organic Lett* 2005;**7**:4269–4272.
15. Huang CY, Thayer DA, Chang AY, *et al.*: Carbohydrate microarray for profiling the antibodies interacting with Globo H tumor antigen. *Proc Natl Acad Sci USA* 2006;103:15–20.
16. Stevens J, Blint O, Glaser L, *et al.*: Glycan microarray analysis of the hemagglutinins from modern and pandemic influenza viruses reveals different receptor specificities. *J Mol Biol* 2006;355:1143–1155.
17. Liang PH, Wang SK, Wong CH: Quantitative analysis of carbohydrate-protein interactions using glycan microarrays: determination of surface and solution dissociation constants. *J Am Chem Soc* 2007;129:11177–11184.
18. Oyelaran O, McShane LM, Dodd L, Gildersleeve JC: Profiling human serum antibodies with a carbohydrate antigen microarray. *J Prot Res* 2009;8:4301–4310.
19. Lam KS, Lebl M, Krchnak V: The one-bead-one-compound combinatorial library method. *Chem Rev* 1997;97:411–448.
20. MacBeath G, Koehler AN, Schreiber SL: Printing small molecules as microarrays and detecting protein-ligand interactions en masse. *J Am Chem Soc* 1999;121: 7967–7968.
21. Xu Q, Lam KS: Protein and chemical microarrays—powerful tools for proteomics. *J Biomed Biotechnol* 2003;5:257–266.
22. Lee M, Shin I: Fabrication of chemical microarrays by efficient immobilization of hydrazide-linked substances on epoxide-coated glass surfaces. *Angew Chem Int Ed Engl* 2005;44:2881–2884.
23. Bradner JE, McPherson OM, Koehler AN: A method for the covalent capture and screening of diverse small molecules in a microarray format. *Nat Protoc* 2006;1:2344–2352.
24. Bradner JE, McPherson OM, Mazitschek R, *et al.*: A robust small-molecule microarray platform for screening cell lysates. *Chem Biol* 2006;13:493–504.
25. Sun YS, Landry JP, Fei YY, *et al.*: Macromolecular scaffolds for immobilizing small molecule microarrays in label-free detection of protein-ligand interactions on solid support. *Analyt Chem* 2009;81:5373–5380.
26. Fei YY, Landry JP, Sun Y, *et al.*: Screening small-molecule compound microarrays for protein ligands without fluorescence labeling with a high-throughput scanning microscope. *J Biomed Opt* 2010;15:016018.
27. Lipshutz RJ, Fodor SP, Gingeras TR, Lockhart DJ: High density synthetic oligonucleotide arrays. *Nat Genet* 1999;21:20–24.
28. Schena M: *Microarray Analysis*. John Wiley & Sons, Hoboken, NJ, 2003.
29. Schena M: *Protein Microarrays*. Jones and Bartlett Publishers, Sudbury, MA, 2004.
30. International Human Genome Sequencing Consortium: Finishing the euchromatic sequence of the human genome. *Nature* 2004;431:931–945.
31. Pennisi E: Working the (gene count) numbers: finally a firm answer. *Science* 2007;316:1113–1113.
32. Harrison PM, Kumar A, Lang N, Snyder M, Gerstein M: A question of size: the eukaryotic proteome and the problems in defining it. *Nucleic Acids Res* 2002;30:1083–1090.
33. Mao H, Graziano JJ, Chase TM, *et al.*: Spatially addressed combinatorial protein libraries for recombinant antibody discovery and optimization. *Nat Biotechnol* 2010;28:1195–1202.
34. Hoogenboom HR: Selecting and screening recombinant antibody libraries. *Nat Biotechnol* 2005;23:1105–1116.
35. Sun YS, Landry JP, Fei YY, *et al.*: Effect of fluorescently labeling protein probes on kinetics of protein-ligand reactions. *Langmuir* 2008;24:13399–13405.
36. Karlsson R, Michaelsson A, Mattsson L: Kinetic analysis of monoclonal antibody-antigen interactions with a new biosensor based analytical system. *J Immunol Methods* 1991;145:229–240.
37. Shumaker-Parry JS, Campbell CT: Quantitative methods for spatially resolved adsorption/desorption measurements in real time by surface plasmon resonance microscopy. *Analyt Chem* 2004;76:907–917.
38. Usui-Aoki K, Shimada K, Nagano M, Kawai M, Koga H: A novel approach to protein expression profiling using antibody microarrays combined with surface plasmon resonance technology. *Proteomics* 2005;5:2396–2401.
39. Rich RL, Myszka DG: Survey of the year 2005 commercial optical biosensor literature. *J Mol Recognit* 2006;19:478–534.
40. Singh BK, Hillier AC: Surface plasmon resonance imaging of biomolecular interactions on a grating-based sensor array. *Anal Chem* 2006;78:2009–2018.
41. Boozer C, Kim G, Cong S, Guan H, Londergan T: Looking towards label-free biomolecular interaction analysis in a high-throughput format: a review of new surface plasmon resonance technologies. *Curr Opin Biotechnol* 2006;17:400–405.
42. Zhu XD: Comparison of two optical techniques for label-free detection of biomolecular microarrays on solids. *Opt Commun* 2006;259:751–753.
43. Piehler J, Brecht A, Gauglitz G, Maul C, Grabley S, Zerlin M: Specific binding of low molecular weight ligands with direct optical detection. *Biosens Bioelectron* 1997;12:531–538.
44. Hanel C, Gauglitz G: Comparison of reflectometric interference spectroscopy with other instruments for label-free optical detection. *Anal Bioanal Chem* 2002;372:91–100.

45. Özkumur E, Needham JW, Bergstein DA, *et al.*: Label-free and dynamic detection of biomolecular interactions for high-throughput microarray applications. *Proc Natl Acad Sci USA* 2008;105:7988–7992.
46. Kurrat R, Textor M, Ramsden JJ, Boni P, Spencer ND: Instrumental improvements in optical waveguide light mode spectroscopy for the study of biomolecule adsorption. *Rev Sci Instrum* 1997;68:2172–2176.
47. Höök, F, Vörös J, Rodahl M, *et al.*: A comparative study of protein adsorption on titanium oxide surfaces using *in situ* ellipsometry, optical waveguide lightmode spectroscopy, and quartz crystal microbalance/dissipation. *Colloids Surf B* 2002;24:155–170.
48. Cross GH, Reeves A, Brand S, *et al.*: The metrics of surface adsorbed small molecules on the Young's fringe dual-slab waveguide interferometer. *J Phys D Appl Phys* 2004;37:74–80.
49. Freeman NJ, Peel LL, Swann MJ, *et al.*: Real time, high resolution studies of protein adsorption and structure at the solid-liquid interface using dual polarization interferometry. *J Phys: Condens Matter* 2004;16:S2493.
50. Arwin H: Ellipsometry on thin organic layers of biological interest: characterization and applications. *Thin Solid Films* 2000;377:48–56.
51. Arwin H: Is ellipsometry suitable for sensor applications? *Sensors Actuators A Phys* 2001;92:43–51.
52. Azzam RMA, Bashara NM: *Ellipsometry and Polarized Light*. North-Holland, Amsterdam, The Netherlands, 1987.
53. Jin G, Jansson R, Arwin H: Imaging ellipsometry revisited: developments for visualization of thin transparent layers on silicon substrates. *Rev Sci Instrum* 1996;67:2930–2936.
54. Wang ZH, Jin G: A label-free multisensing immunosensor based on imaging ellipsometry. *Analyt Chem* 2003;75:6119–6123.
55. Landry JP, Zhu XD, Gregg JP: Label-free detection of microarrays of biomolecules by oblique-incidence reflectivity difference microscopy. *Opt Lett* 2004;29:581–583.
56. Landry JP, Sun YS, Guo XW, Zhu XD: Protein reactions with surface-bound molecular targets detected by oblique-incidence reflectivity difference microscopes. *Appl Opt* 2008;47:3275–3288.
57. Fei YY, Landry JP, Sun YS, *et al.*: A novel high-throughput scanning microscope for label-free detection of protein and small-molecule chemical microarrays. *Rev Sci Instrum* 2008;79:013708.
58. Zhu XD, Landry JP, Sun YS, Gregg JP, Lam KS, Guo X: Oblique-incidence reflectivity difference microscope for label-free high-throughput detection of biochemical reactions in a microarray format. *Appl Opt* 2007; 46:1890–1895.
59. Landry JP, Zhu XD, Gregg JP, Guo XW: Detection of biomolecular microarrays without fluorescent-labeling agents. *Proc SPIE* 2004;5328:121–128.
60. Thomas P, Nabighian E, Bartelt MC, Fong CY, Zhu XD: An oblique-incidence optical reflectivity difference and LEED study of rare-gas growth on a lattice-mismatched metal substrate. *Appl Phys A* 2004;79:131–137.
61. Sober HA: *Handbook of Biochemistry: Selected Data for Molecular Biology*. Chemical Rubber Co., Cleveland, OH, 1970.
62. Sreenath K, Prabhasankar P, Venkatesh YP: Generation of an antibody specific to erythritol, a non-immunogenic food additive. *Food Addit Contam* 2006; 23:861–869.
63. Morton TA, Myszka DG, Chaiken IM: Interpreting complex binding kinetics from optical biosensors: a comparison of analysis by linearization, the integrated rate equation, and numerical integration. *Analyt Biochem* 1995; 227:176–185.
64. Myszka DG, Arulanatham PR, Sana T, Wu Z, Morton TA, Ciardelli TL: Kinetic analysis of ligand binding to interleukin-2 receptor complexes created on an optical biosensor surface. *Protein Sci* 1996;5:2468–2478.
65. Schuck P: Reliable determination of binding affinity and kinetics using surface plasmon resonance biosensors. *Curr Opin Biotechnol* 1997;8:498–502.
66. Jung H, Yang T, Lasagna MD, Shi J, Reinhart GD, Cremer PS: Impact of hapten presentation on antibody binding at lipid membrane interfaces. *Biophys J* 2008;94:3094–3103.
67. Adamczyk H, Mattingly PG, Shrender K, Yu Z: Surface plasmon resonance (SPR) as a tool for antibody conjugate analysis. *Bioconjugate Chem* 1999; 10:1032–1037.
68. MacBeath G: Protein microarrays and proteomics. *Nat Genet* 2002;32:526–532.

Address correspondence to:
Xiangdong Zhu, PhD
Department of Physics
University of California at Davis
Davis, CA 95616

E-mail: xdzhu@physics.ucdavis.edu

Simultaneous Measurement of 10,000 Protein-Ligand Affinity Constants Using Microarray-based Kinetic Constant Assays

J. P. Landry, Y. Y. Fei, and X. D. Zhu*

Department of Physics, University of California at Davis, Davis, California, 95616, USA

* Corresponding Author, xdzhu@physics.ucdavis.edu

SUPPLEMENTAL MATERIALS

OI-RD Scanning Microscope Control

Microscope control, data acquisition, image processing/analysis, binding curve processing/analysis (nonlinear curve fitting), and report generation are performed with a custom application suite developed in LabVIEW 7 (National Instruments, Austin, TX) by ourselves.

Microarray Printing Conditions

The microarrays were printed at ambient temperature (~ 25°C) and elevated relative humidity (~ 65%). The target materials were dissolved in 1× PBS (pH 7.5) to desired concentrations for printing. Primary amines on the target protein surface bind covalently to the epoxide groups on the glass surface. The printing robot was equipped with eight silicon 100 μm quill pins (Parallel Synthesis, Santa Clara, CA). The centers of the printed spots were separated by 250 μm and the diameters of the spots varied from 80 μm to 160 μm depending on the concentration and the wetting properties of the printed solution. The printed microarrays were stored in a slide box for a minimum of 12 hours before further processing.

K_a Maps of Eight Protein Probes Against the 10,880-spot Target Microarrays Shown in Fig. 5

We measured binding curves of eight protein probes against the 10,880-spot target microarray (**Figure 5**) by sequentially exposing the microarray to solutions of these probes at one

concentration. In order of reactions, the 8 protein probes were anti-phenobarbital IgG, concanavalin A (lectin), anti-theophylline IgG, anti-biotin IgG, anti-tetrahydrocannabinol IgG, anti-morphine IgG, anti-dinitrophenol IgG, and anti-methamphetamine IgG. We repeated the reaction sequence with different probe concentrations on fresh microarrays to obtain 10,880 sets of binding curves for each printed target. **Figure S-1** through **Figure S-8** display K_a maps (equilibrium association constants) of these eight proteins against the 10,880 targets, representative sets of binding curves for each probe, and the histogram of K_a for each probe against the same specific targets but printed at different locations. We show the means and the standard deviations of the association rates, dissociation rates, and equilibrium association constants of eight specific probe-target pairs in Table 1.

It is clear that there is noticeable cross reactivity of mouse anti-theophylline IgG to dinitrophenol-BSA targets, albeit with an order of magnitude smaller K_a. For concanavalin A, in addition to specific binding to glucose-BSA targets, the protein also binds to a number of immobilized IgG targets.

FIGURE S-1

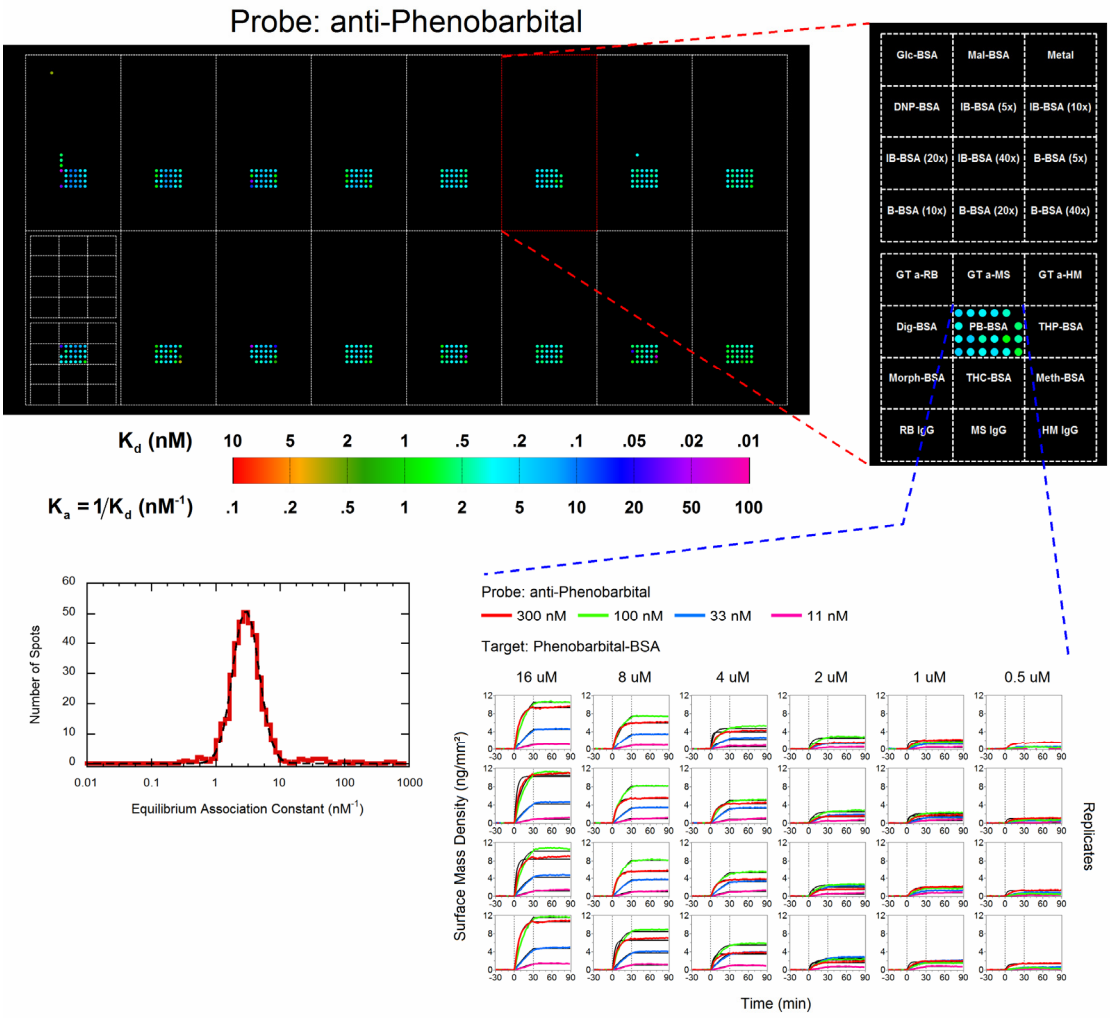
Probe: anti-Phenobarbital
Glc-BSA
Mal-BSA
Metal
DNP-BSA
IB-BSA (5x)
IB-BSA (10x)
IB-BSA (20x)
IB-BSA (40x)
B-BSA (5x)
B-BSA (10x)
B-BSA (20x)
B-BSA (40x)
GT a-RB
GT a-MS
GT a-HM
Dig-BSA
PB-BSA
THP-BSA
Morph-BSA
THC-BSA
Meth-BSA
RB IgG
MS IgG
HM IgG
K_d (nM) 10 5 2 1 .5 .2 .1 .05 .02 .01
K_a = 1/K_d (nM^-1) .1 .2 .5 1 2 5 10 20 50 100
Number of Spots
Equilibrium Association Constant (nM^-1)
Probe: anti-Phenobarbital
300 nM
100 nM
33 nM
11 nM
Target: Phenobarbital-BSA
16 uM
8 uM
4 uM
2 uM
1 uM
0.5 uM
Surface Mass Density (ng/mm²)
Replicates
Time (min)

FIGURE S-2

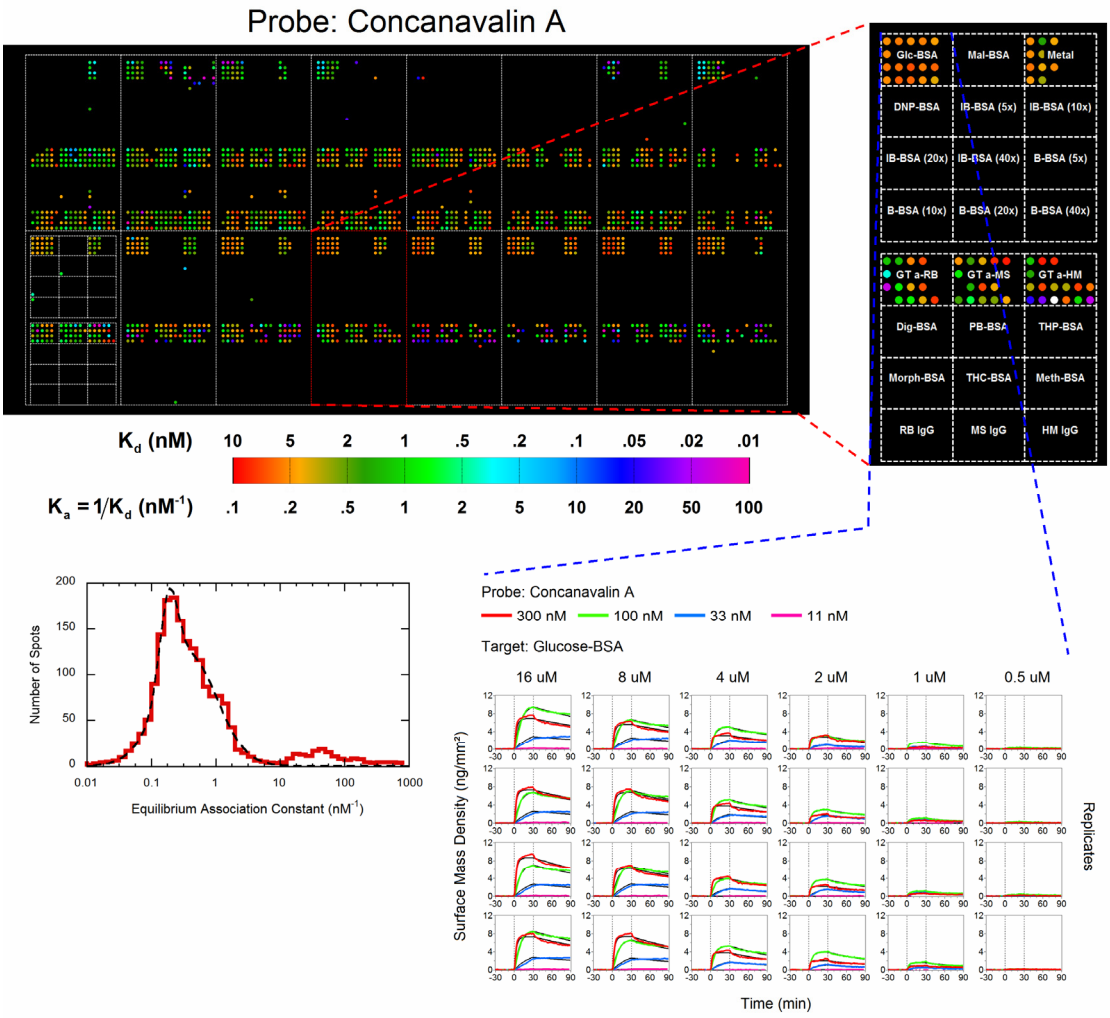
Probe: Concanavalin A
Glc-BSA
Mal-BSA
Metal
DNP-BSA
IB-BSA (5x)
IB-BSA (10x)
IB-BSA (20x)
IB-BSA (40x)
B-BSA (5x)
B-BSA (10x)
B-BSA (20x)
B-BSA (40x)
GT a-RB
GT a-MS
GT a-HM
Dig-BSA
PB-BSA
THP-BSA
Morph-BSA
THC-BSA
Meth-BSA
RB IgG
MS IgG
HM IgG
Kd (nM) 10 5 2 1 .5 .2 .1 .05 .02 .01
Ka = 1/Kd (nM-1) .1 .2 .5 1 2 5 10 20 50 100
Number of Spots
Equilibrium Association Constant (nM-1)
Probe: Concanavalin A
300 nM
100 nM
33 nM
11 nM
Target: Glucose-BSA
16 uM
8 uM
4 uM
2 uM
1 uM
0.5 uM
Surface Mass Density (ng/mm²)
Replicates
Time (min)

FIGURE S-3

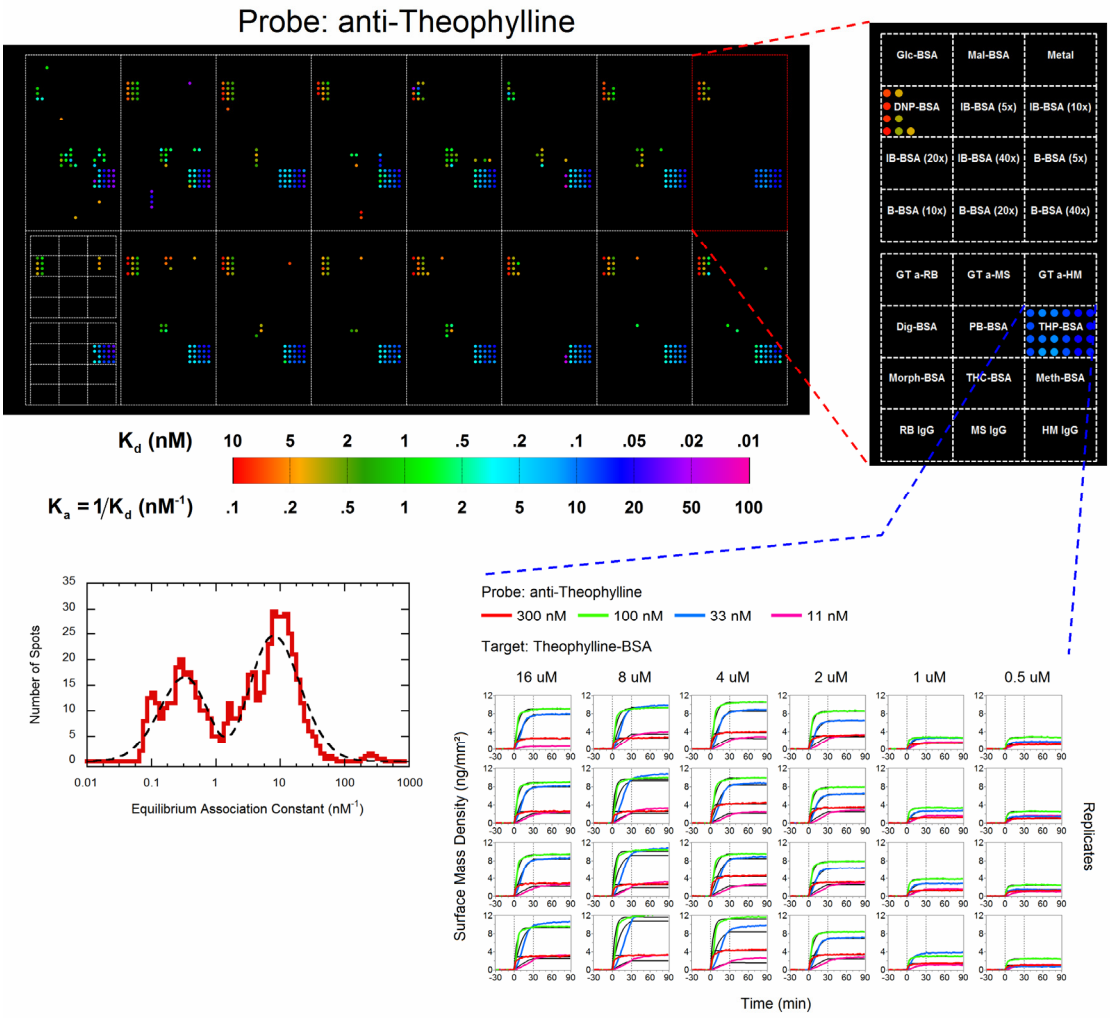
Probe: anti-Theophylline
Glc-BSA
Mal-BSA
Metal
DNP-BSA
IB-BSA (5x)
IB-BSA (10x)
IB-BSA (20x)
IB-BSA (40x)
B-BSA (5x)
B-BSA (10x)
B-BSA (20x)
B-BSA (40x)
GT a-RB
GT a-MS
GT a-HM
Dig-BSA
PB-BSA
THP-BSA
Morph-BSA
THC-BSA
Meth-BSA
RB IgG
MS IgG
HM IgG
K_d (nM) 10 5 2 1 .5 .2 .1 .05 .02 .01
K_a = 1/K_d (nM^-1) .1 .2 .5 1 2 5 10 20 50 100
Number of Spots
Equilibrium Association Constant (nM^-1)
Probe: anti-Theophylline
300 nM
100 nM
33 nM
11 nM
Target: Theophylline-BSA
16 uM
8 uM
4 uM
2 uM
1 uM
0.5 uM
Surface Mass Density (ng/mm²)
Replicates
Time (min)

FIGURE S-4

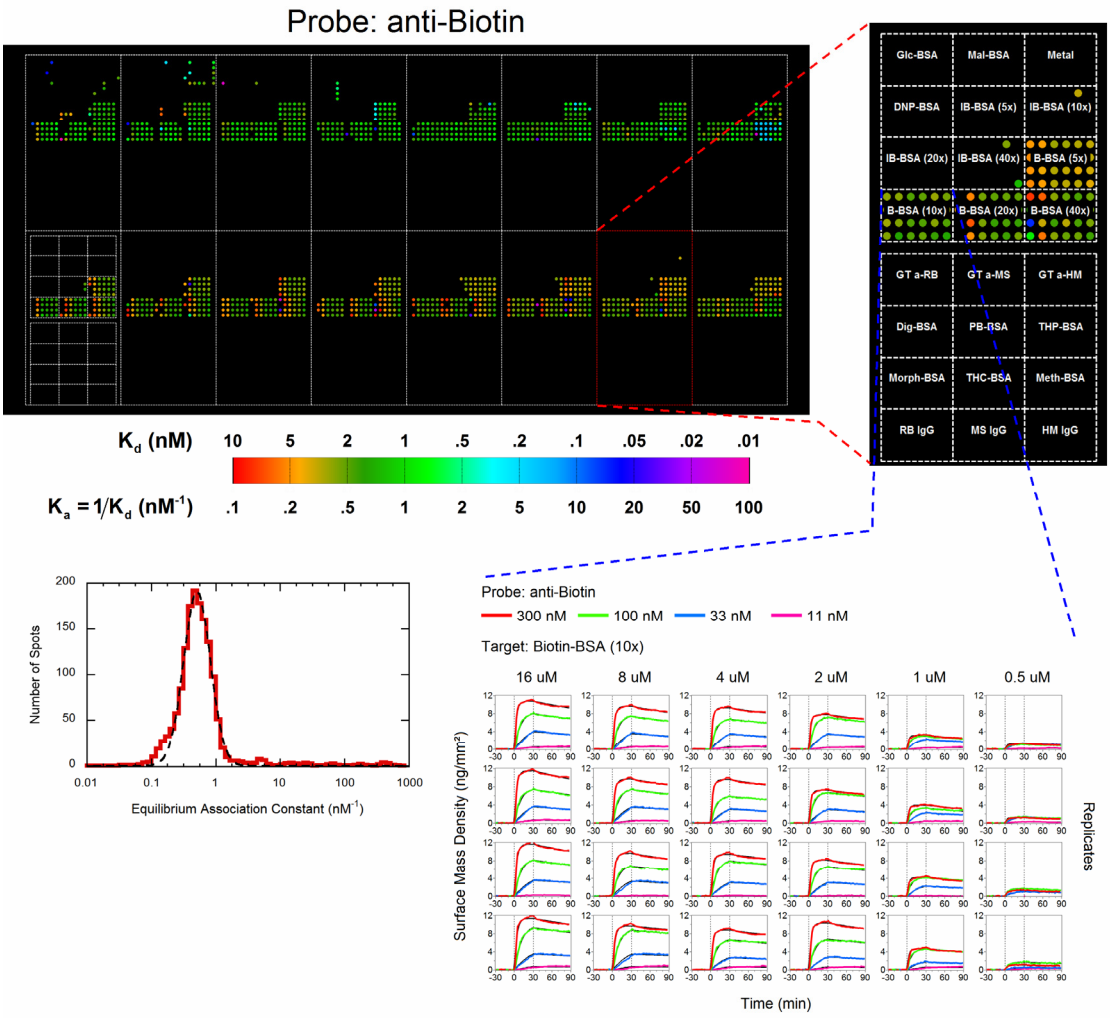
Probe: anti-Biotin
Glc-BSA
Mal-BSA
Metal
DNP-BSA
IB-BSA (5x)
IB-BSA (10x)
IB-BSA (20x)
IB-BSA (40x)
B-BSA (5x)
B-BSA (10x)
B-BSA (20x)
B-BSA (40x)
GT a-RB
GT a-MS
GT a-HM
Dig-BSA
PB-BSA
THP-BSA
Morph-BSA
THC-BSA
Meth-BSA
RB IgG
MS IgG
HM IgG
Kd (nM) 10 5 2 1 .5 .2 .1 .05 .02 .01
Ka = 1/Kd (nM-1) .1 .2 .5 1 2 5 10 20 50 100
Number of Spots
Equilibrium Association Constant (nM-1)
Probe: anti-Biotin
300 nM
100 nM
33 nM
11 nM
Target: Biotin-BSA (10x)
16 uM
8 uM
4 uM
2 uM
1 uM
0.5 uM
Surface Mass Density (ng/mm²)
Replicates
Time (min)

FIGURE S-5

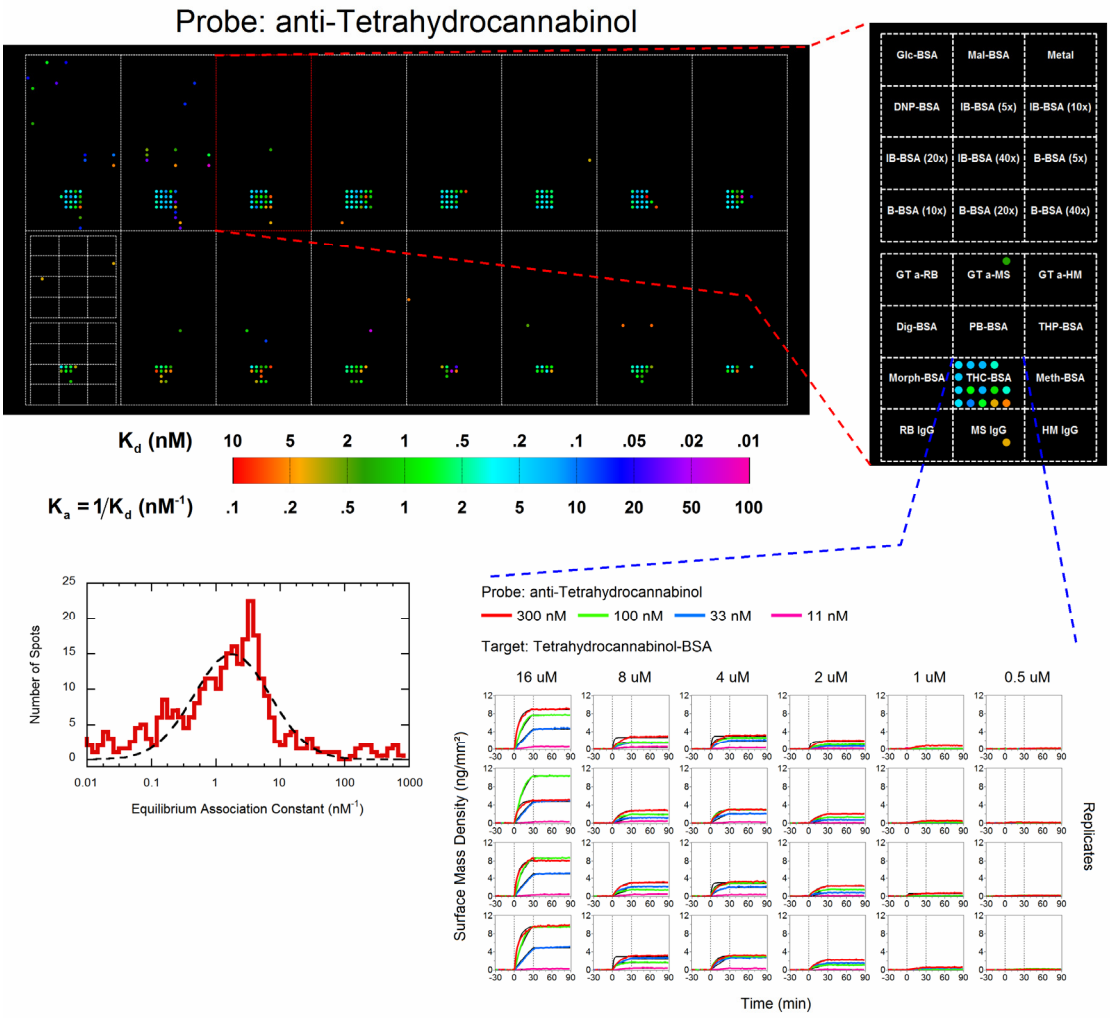
Probe: anti-Tetrahydrocannabinol
Glc-BSA
Mal-BSA
Metal
DNP-BSA
IB-BSA (5x)
IB-BSA (10x)
IB-BSA (20x)
IB-BSA (40x)
B-BSA (5x)
B-BSA (10x)
B-BSA (20x)
B-BSA (40x)
GT a-RB
GT a-MS
GT a-HM
Dig-BSA
PB-BSA
THP-BSA
Morph-BSA
THC-BSA
Meth-BSA
RB IgG
MS IgG
HM IgG
K_d (nM) 10 5 2 1 .5 .2 .1 .05 .02 .01
K_a = 1/K_d (nM^-1) .1 .2 .5 1 2 5 10 20 50 100
Number of Spots
Equilibrium Association Constant (nM^-1)
Probe: anti-Tetrahydrocannabinol
300 nM
100 nM
33 nM
11 nM
Target: Tetrahydrocannabinol-BSA
16 uM
8 uM
4 uM
2 uM
1 uM
0.5 uM
Surface Mass Density (ng/mm²)
Replicates
Time (min)

FIGURE S-6

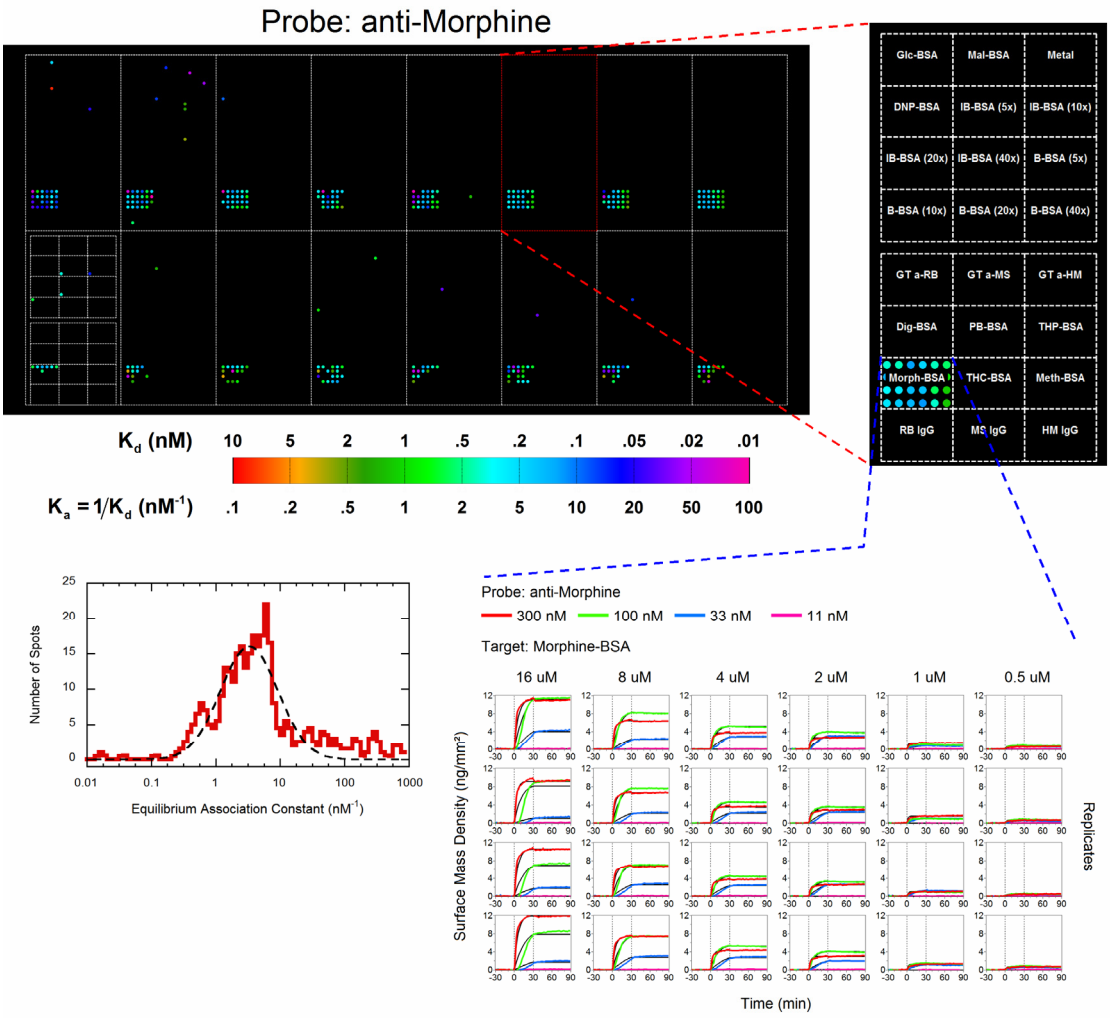
Probe: anti-Morphine
Glc-BSA
Mal-BSA
Metal
DNP-BSA
IB-BSA (5x)
IB-BSA (10x)
IB-BSA (20x)
IB-BSA (40x)
B-BSA (5x)
B-BSA (10x)
B-BSA (20x)
B-BSA (40x)
GT a-RB
GT a-MS
GT a-HM
Dig-BSA
PB-BSA
THP-BSA
Morph-BSA
THC-BSA
Meth-BSA
RB IgG
MS IgG
HM IgG
K_d (nM) 10 5 2 1 .5 .2 .1 .05 .02 .01
K_a = 1/K_d (nM^-1) .1 .2 .5 1 2 5 10 20 50 100
Number of Spots
Equilibrium Association Constant (nM^-1)
Probe: anti-Morphine
300 nM
100 nM
33 nM
11 nM
Target: Morphine-BSA
16 uM
8 uM
4 uM
2 uM
1 uM
0.5 uM
Surface Mass Density (ng/mm²)
Replicates
Time (min)

FIGURE S-7

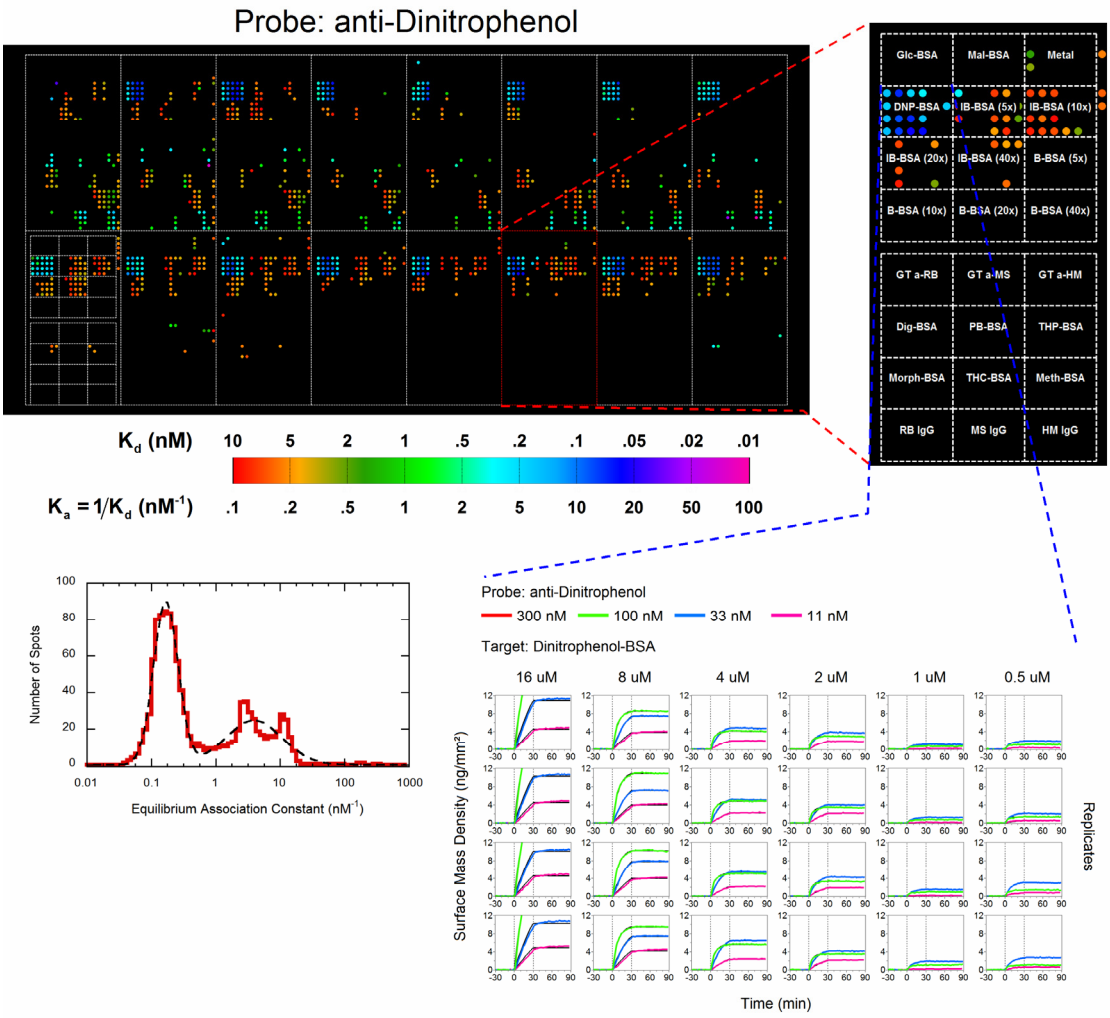
Probe: anti-Dinitrophenol
Glc-BSA
Mal-BSA
Metal
DNP-BSA
IB-BSA (5x)
IB-BSA (10x)
IB-BSA (20x)
IB-BSA (40x)
B-BSA (5x)
B-BSA (10x)
B-BSA (20x)
B-BSA (40x)
GT a-RB
GT a-MS
GT a-HM
Dig-BSA
PB-BSA
THP-BSA
Morph-BSA
THC-BSA
Meth-BSA
RB IgG
MS IgG
HM IgG
Kd (nM) 10 5 2 1 .5 .2 .1 .05 .02 .01
Ka = 1/Kd (nM-1) .1 .2 .5 1 2 5 10 20 50 100
Number of Spots
Equilibrium Association Constant (nM-1)
Probe: anti-Dinitrophenol
300 nM
100 nM
33 nM
11 nM
Target: Dinitrophenol-BSA
16 uM
8 uM
4 uM
2 uM
1 uM
0.5 uM
Surface Mass Density (ng/mm²)
Replicates
Time (min)

FIGURE S-8

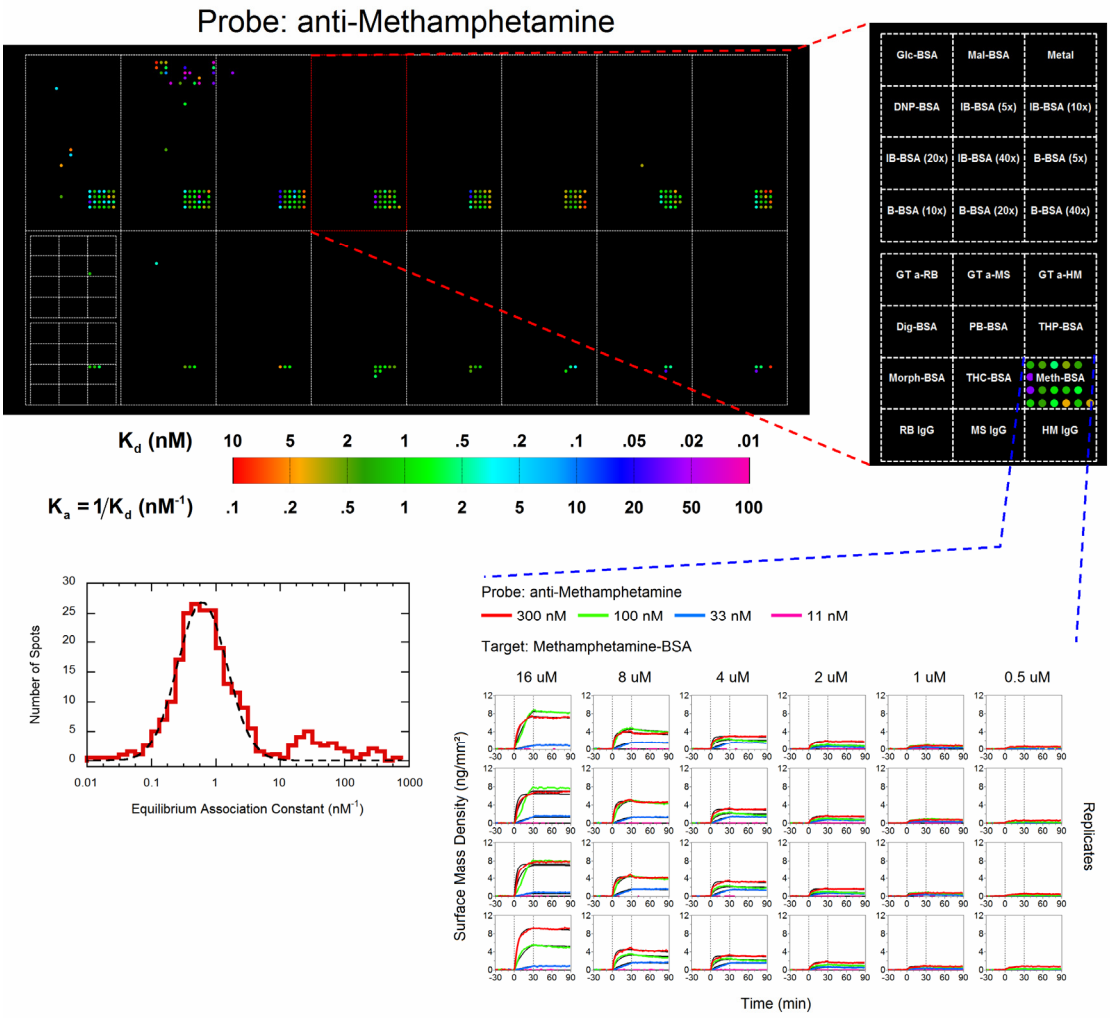
Probe: anti-Methamphetamine
Glc-BSA
Mal-BSA
Metal
DNP-BSA
IB-BSA (5x)
IB-BSA (10x)
IB-BSA (20x)
IB-BSA (40x)
B-BSA (5x)
B-BSA (10x)
B-BSA (20x)
B-BSA (40x)
GT a-RB
GT a-MS
GT a-HM
Dig-BSA
PB-BSA
THP-BSA
Morph-BSA
THC-BSA
Meth-BSA
RB IgG
MS IgG
HM IgG
K_d (nM) 10 5 2 1 .5 .2 .1 .05 .02 .01
K_a = 1/K_d (nM^-1) .1 .2 .5 1 2 5 10 20 50 100
Number of Spots
Equilibrium Association Constant (nM^-1)
Probe: anti-Methamphetamine
300 nM
100 nM
33 nM
11 nM
Target: Methamphetamine-BSA
16 uM
8 uM
4 uM
2 uM
1 uM
0.5 uM
Surface Mass Density (ng/mm²)
Replicates
Time (min)

TABLE S-1: Association rates, dissociation rates, and equilibrium association constants of eight protein probes with respective ligands (**Figure 5**). The values are 68% confidence intervals obtained from the mean and standard deviation of a Gaussian distribution fit to a histogram of values from *all* appropriate microarray spots (several hundred spots for each reaction). Values for each spot were obtained from nonlinear curve fitting to the Langmuir binding reaction model. We estimate from the data a 68% confidence *upper bound* for the dissociation rate (the association and dissociation rates must be nonnegative) where appropriate. They are comparable in value to the available affinity constants for some of monoclonal mouse anti-drug IgG molecules that Fitzgerald Industries International, Inc. provides commercially (http://www.fitzgerald-fii.com/Products?pId=9&sId=21).

Probe	Target	k_{on} $(M \cdot s)^{-1}$	k_{off} (s^{-1})	K_a (nM^{-1})
anti-phenobarbital IgG	phenobarbital-BSA	$(1.3 \pm 0.1) \times 10^4$	$< 4.8 \times 10^{-6}$	> 2.7
concanavalin A	glucose-BSA	$(2.3 \pm 0.3) \times 10^4$	$(8.7 \pm 0.9) \times 10^{-5}$	0.26 ± 0.01
	whole IgG	$(1.00 \pm 0.07) \times 10^4$	$(2.2 \pm 0.4) \times 10^{-5}$	0.45 ± 0.07
anti-theophylline IgG	theophylline-BSA	$(3.4 \pm 0.3) \times 10^4$	$< 2.8 \times 10^{-6}$	> 11
	dinitrophenol-BSA	$(3.4 \pm 0.3) \times 10^4$	$(9 \pm 3) \times 10^{-5}$	0.36 ± 0.01
anti-biotin IgG	biotin-BSA	$(2.2 \pm 0.2) \times 10^4$	$(4.5 \pm 0.5) \times 10^{-5}$	0.53 ± 0.06
anti-tetrahydrocannabinol IgG	tetrahydrocannabinol-BSA	$(1.1 \pm 0.2) \times 10^4$	$< 9.1 \times 10^{-6}$	> 1.2
anti-morphine	morphine-BSA	$(2.1 \pm 0.2) \times 10^4$	$< 6.9 \times 10^{-6}$	> 3.0
anti-dinitrophenol	dinitrophenol-BSA	$(1.8 \pm 0.1) \times 10^4$	$< 7.2 \times 10^{-6}$	> 2.5
anti-methamphetamine	methamphetamine-BSA	$(1.6 \pm 0.2) \times 10^4$	$(2.2 \pm 0.4) \times 10^{-5}$	0.72 ± 0.1

Measurement of Reflectivity Phase Difference $\Delta\delta$

In this section, we provide details on how the OI-RD microscope measures the changes in the reflectivity phase δ, where $r_p/r_s = \tan\psi \cdot \exp(i\delta)$ and r_p and r_s are the complex *p*-polarized and *s*-polarized reflectivities, respectively. This microscope varies in several details from previously reported OI-RD microscopes[1-4]. In particular, this microscope is designed to measure changes in δ exclusively (previous microscopes can also measure changes in ψ). Since the OI-RD response with optically transparent substrates and protein layers is predominantly through δ, the current microscope configuration sacrifices very little information in exchange for a simpler and more robust signal normalization scheme compared to previous OI-RD microscopes. However, it should be pointed out that the high-speed scanning mechanisms are independent of these details and therefore high-throughput kinetic measurements analogous to those described in the main text can be performed with the previous OI-RD configurations as well.

The arrangement of the optics in the OI-RD microscope is illustrated in Figure 1 and (for convenience) **Figure S-9** (top). A He-Ne laser beam of wavelength λ = 633 nm and linearly polarized at angle *P* (from *p*-polarization) passes through a photoelastic modulator (PEM). The photoelastic modulator acts as a waveplate with a sinusoidally varying retardation of frequency Ω = 50 kHz and amplitude $\pi/2$ (quarter wave). The axes of the PEM are aligned with the glass slide *p*- and *s*-polarization components. The beam passes through a phase shifter (e.g. a wave plate tilted about a principal axis) that adds an adjustable but static phase Φ_{PS} between the *p*- and *s*-polarized components. The scan lens focuses the beam into a ~ 30 μm diameter spot on the microarray-bearing glass surface at incidence angle $\theta = 36.6°$ inside the glass slide. The microarray-bearing surface is immersed in an aqueous solution within the flow channel. The reflected beam from the illuminated spot passes through an analyzer with its transmission axis set at angle *A* (from *p*-polarization) and is imaged with an objective lens onto a long-profile photodiode. A slit in front of the photodiode passes the image from the back surface reflection and blocks the images from the front surface reflection and from multiple bounces within the glass slide. The first and second harmonic components of the resulting photocurrent are measured with lock-in amplifiers. Their signed amplitudes are

$$S(\Omega) = -I_0 J_1(\pi) H(\Omega) |r_p| |r_s| \sin(2P) \sin(2A) \sin(\delta + \Phi_{PS} + \Phi_{sys}) \quad \text{(S-1)}$$

for the first harmonic and

$$S(2\Omega) = I_0 J_2(\pi) H(2\Omega) |r_p| |r_s| \sin(2P) \sin(2A) \cos(\delta + \Phi_{PS} + \Phi_{sys}) \quad \text{(S-2)}$$

for the second harmonic. The other symbols in these expressions are as follows: I_0 is the output intensity of the laser; J_1 and J_2 are Bessel functions of the first kind; H is the frequency-dependent proportionality between the laser intensity amplitude at the photodiode and the measured photocurrent amplitude; $|r_p|$ and $|r_s|$ are the products of the *p*- and *s*-polarization reflection/transmission coefficient magnitudes for all the surfaces in the system (including the microarray surface); δ is the phase difference between the *p*- and *s*-polarized components due to reflection from the microarray surface; Φ_{PS} is the phase difference due to the phase shifter; and Φ_{sys} is the phase difference due to all the other components. Let $\eta = S_{\max}(\Omega)/S_{\max}(2\Omega)$ where $S_{\max}(\Omega) = -I_0 J_1(\pi) H(\Omega) \sin(2P) \sin(2A)$ $S_{\max}(2\Omega) = I_0 J_2(\pi) H(2\Omega) \sin(2P) \sin(2A)$. The parameter η is independent of the properties of the microarray surface and can be determined by measuring the amplitudes of $S(\Omega)$ and $S(2\Omega)$ plotted as a function of Φ_{PS}. This only needs to be done once because those factors that do not divide out in the ratio remain constant throughout use of the microscope. With these definitions $S(\Omega) = \eta S_{\max}(2\Omega) |r_p| |r_s| \sin(\delta + \Phi_{PS} + \Phi_{sys})$ and $S(2\Omega) = S_{\max}(2\Omega) |r_p| |r_s| \cos(\delta + \Phi_{PS} + \Phi_{sys})$. Next, let δ_0 be the phase difference for a bare (unprinted) region of the microarray surface. We initially adjust Φ_{PS} so that $\delta_0 + \Phi_{PS} + \Phi_{sys} = 0$ (or, more generally, a multiple of π), giving $S(\Omega) = 0$ and $S(2\Omega) = S_{\max}(2\Omega) |r_p| |r_s|$. When a thin layer of molecules is subsequently added to the bare surface or when the focused beam is moved to a microarray spot, the photocurrent amplitudes become $S(\Omega) \approx \eta S_{\max}(2\Omega) |r_p| |r_s| (\delta - \delta_0)$ and $S(2\Omega) \approx S_{\max}(2\Omega) |r_p| |r_s|$. Therefore, under this "nulling" condition of the first harmonic, the phase difference $\Delta\delta = \delta - \delta_0$ is obtained from the measured amplitudes by $\Delta\delta = S(\Omega)/[\eta S(2\Omega)]$. Before each image or real-time scan, the first harmonic is "nulled" as described above at a reference location on the unprinted microarray substrate.

FIGURE S-9

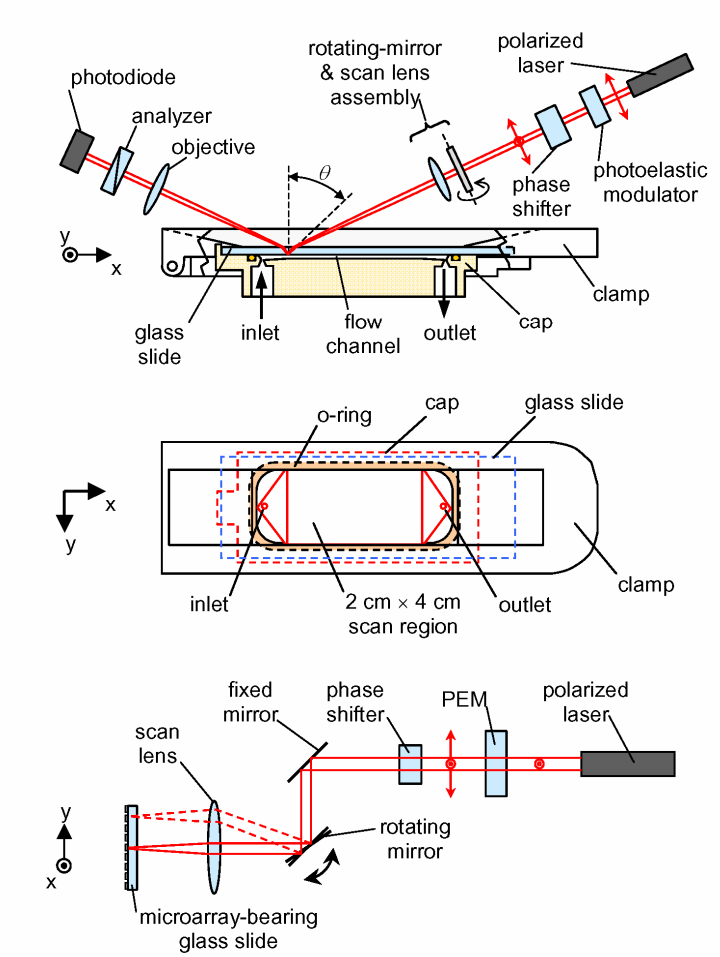

Top panel: Optical layout of the scanning OI-RD microscope. A glass slide with a microarray printed on the bottom surface is installed in a flow channel assembly. A polarization-modulated laser beam is scanned across the microarray in the *y*-direction for y-scan with a combination of a rotating mirror and a scan lens, while the flow channel assembly is translated in the *x*-direction relative to the illumination optics for x-scan. **Middle panel:** bottom view of the flow chamber assembly showing the 2 cm × 4 cm optically accessible area on the glass slide. **Bottom panel:** side view of the scanning microscope illustrating the *y*-scan.

Optimizing Spot Locations for Real-time Readout

For fast real-time readout, it is essential that the encoded linear translation stage (*x*-direction in **Figure 1** and **Figure S-9**) does not stop much more often than the number of columns in a microarray. As a result, it is crucial that the centers of printed spots along a microarray column (fast scan direction, *y* direction) do not deviate from a straight line by more than the spot radii so that the fast rotating mirror raster scan can be performed at one *x*-coordinate per microarray column, instead of many *x*-coordinates for a single column of targets. Three factors affect this: (1) the diameter and morphology of printed spots, (2) the precision of the printing robot, and (3) the regularity of pin diameters and pin-to-pin separation in the print head. Item (1) is the most variable because it depends on the physicochemical properties of the glass slide surface, the printing buffer, and the dissolved target. For example, in the first experiment described in the main text the printed BSA spots had diameters ranging from 120 μm to 140 μm. In the second experiment, the range was even larger when printing concentrations were varied. By printing a large microarray with a single pin (data not shown), we found that the standard deviation of the spot spacing was 9 μm due to robotic motion precision, close to the nominal 2.5 μm digital encoder resolution of the OmniGrid 100 translation motors. For high-throughput printing of many replicate microarrays (up to 100), multiple pins must be employed. Since a readout line needs to pass through all the spots in a column printed with different pins so that the encoded linear stage only needs to stop once for the row, the centers of the pins in the print head cannot deviate from a straight line by more than the spot radius. Typical stainless steel pins used in most robotic microarray printers do not have such a precise pin-to-pin alignment. We found that silicon pins and the associated print head from Parallel Synthesis Inc (San Jose, CA) had the pin-to-pin alignment precision for our application. Our printing test showed that the standard deviation of spot centers printed with 8 silicon pins was 11 μm, so that 99 % of the printed spot centers will fall within 55 μm, less than one half of the spot diameter. This regularity in spot center position allows convenient specification of the readout grid and in turn enables high-speed real-time readout.

OI-RD Image Processing

The goal of microarray image analysis is to report the amount of probe-target complex formed at each spot of the microarray. For fluorescence images, this goal is achieved with the following strategies: (1) determine a grid for addressing each spot, (2) segment spot pixels from background pixels, (3) determine if a given spot location contains a valid endpoint signal, and (4) calculate the signal from the spot pixels and the local background. These strategies remain the same in principle for OI-RD images of large microarrays, yet differ significantly in implementation. First, fluorescence signals are represented by non-negative values (typically unsigned 16-bit integers and expressed in instrument-dependent arbitrary units). The OI-RD signals may take positive and negative values and although the raw OI-RD signals are acquired by digitizing an analog signal (at 16-bit resolution), the signals have an instrument-independent physical interpretation according to Eq. (1) (see the main text). Thus, it is most useful to process the OI-RD signals as floating-point values.

A second important difference is the nature of the background signals in these two types of microarray images. Fluorescence, by its nature, allows sensitive discrimination of appropriately labeled molecules. Background from autofluorescence, nonspecific binding, and artifacts such as smearing of target molecules during washing steps ("comet tails") inevitably occur, but can be minimized in principle by optimizing the microarray fabrication and reaction protocols. After gridding and segmenting spot pixels, the typical approach to quantifying fluorescence endpoints is to subtract an average of the local background pixels from an average of the spot pixels. In contrast, *all* label-free optical detection methods, including OI-RD and surface plasmon resonance imaging, are subject to all processes that can change the phase and magnitude of a reflected optical beam. Thus, for OI-RD images, it is important to correct (subtract out) the background both globally and locally before assessing the signal of a target spot.

The third important difference is that gridding and normalization of the spot signals are often the most difficult step in fluorescence image analysis. This is because the image quantifying the *target* microarray is usually unavailable; the structure of the grid and the target density of each spot

must be deduced from one or more probe reactions. For OI-RD images, it is routine to obtain high-contrast images of a target microarray (either before or after washing away excess printed material) before reaction with a probe. As a result, the target spots are relatively easily located and gridded, greatly aiding the process of background correction necessary for OI-RD images (the most difficult step in OI-RD image analysis). We next describe the semi-automated procedures used to process OI-RD images acquired for this study.

Grid Determination

The printed, yet unprocessed microarray is installed in the microscope and scanned. The reflectance signal $\delta R_p/R_p + \delta R_s/R_s$, with $R_p = |r_p|^2$ and $R_s = |r_s|^2$ (available as the second harmonic of the polarization-modulated laser intensity in reflection), from the spots are large with almost negligible background. A line is drawn between the centroids of the bottom-left and bottom-right spots in the microarray (see **Figure 2**, main text) to determine the angle of the microarray relative to the scan axes. Angular deviations larger than one milliradian are corrected by rotating the fluidic chamber assembly with a flexure-tilt mechanism.

First iteration readout grid. Once the microarray axes are aligned with the scan axes, the reflectance signals $\delta R_p/R_p + \delta R_s/R_s$ are added up along the *y*-axis (image pixel columns) to obtain a comb-like profile of *x*-coordinates, and the same signals are added up along the *x*-axis (image pixel rows) to obtain a comb-like profile of *y*-coordinates. The peak positions in these two profiles mark the average coordinates of printed spots on a rectangular grid, albeit irregularly spaced. These positions are found by fitting a quadratic equation to the profile points located in a sliding window. The fit coefficients are tested to see if the quadratic is consistent with a local maximum of sufficient height and width, and if so the peak location is calculated. These peak positions in *x* and *y* coordinates form the first iteration of the real-time readout grid. After the target channel pixels (grid points) are located, the reference channel pixels are determined by computing the midpoint between consecutive targets in the *y* (fast scan) direction; references at the edges of the arrays are positioned approximately half a spot spacing away.

Second iteration readout grid. If there is a great deal of variability in the spot diameters and the locations of the spot centroids, the average coordinates as specified in the first-iteration readout grid can miss a significant number of target spots. In this case, we make the following adjustments: The reflectance image is globally binarized (with thresholds set to the global image mean ± one standard deviation) to segment out the spots. The image is then partitioned into rectangles centered on the original grid points, each containing a binarized target spot. We shift the readout coordinates for the spot from the geometrical center of the rectangle to the centroid of the binarized spot (if a spot is not present, the center of the box is used). These shifted coordinates form the second iteration readout grid. Our scanning software can read out this "center-of-mass relaxed" grid in real-time, and the algorithm works extremely well for small microarrays. But for large microarrays with 10,000 spots such a "center-of-mass relaxed" readout grid with a nearly random distribution of pixel positions is inefficient due to the large number of distinct x coordinates (up to 10,000 from less than 200) where the encoded linear stage needs to stop.

Third iteration readout grid. Thus for large microarrays, we choose the median of the "center-of-mass relaxed" x coordinates for each column of the printed targets (parallel to y axis) as the x-coordinate for the entire row, thus reducing the number of distinct target x coordinates from potentially 10,000 back to the number of target rows. Since scanning along the y direction is accomplished with a fast scan mirror, the unique y values can be kept without significant increase in total readout time. For operational reasons though, we sometimes choose the median of the "center-of-mass relaxed" y coordinates as the y-coordinates for a column of printed targets.

Background Correction

In order of decreasing length scale, the background signals in an OI-RD image (the $\Delta\delta$ phase signal from the measurement of the first harmonic of the reflected laser beam in polarization modulation frequency) are: (1) a monotonic and nearly linear component arising from the change in incidence angle with respect to the scan mirror surface; (2) mechanical strain in the glass substrate (recall the substrate is used as a window to the flow cell); (3) inhomogeneity on the glass surface and

chemically functionalized surface coating; and (4) stochastic pixel-to-pixel noise. Nominally, backgrounds (1)-(3) are static in time and are unaffected by a reaction of the microarray. Thus, the simple means of background correction is to *subtract* an image taken before a reaction from an image taken after the reaction, revealing the change due only to the reaction (plus noise). However, in practice these backgrounds (particularly item (2)) slowly drift in time, leaving a residual background in the difference image that must be corrected. Furthermore, if one desires to extract quantitative information from a target image, these backgrounds must be corrected. Generally, our background correction results are more accurate and robust for difference images due to smaller background signals.

We start with reducing background (1) by modeling it with a 3rd-order two-dimensional polynomial and subtracting it pixel-by-pixel from the image. Let us denote the original $\Delta\delta$ image as Image-0. Because the image is large, we do not wish to perform a computationally expensive least-squares calculation on all of the pixels. Thus, we first create a coarse-grained version of Image-0, which we will denote as Image-1. To obtain Image-1, we interpolate each row of pixels in Image-0 with cubic splines, select a sparse set of regularly spaced points along the rows (e.g. one tenth of the original pixel density along both directions), and evaluate the interpolating functions at these new locations; the process is then repeated for the other direction (pixel columns). On Image-1, we then apply simple thresholds (global image median ± three median absolute deviations) to crudely segment out the strongest microarray spots and artifacts (air bubbles, scratches, dirt) remaining in the coarse grained image. We least squares fit the coarse grained image globally to a 3rd-order two-dimensional polynomial, excluding the segmented pixels from the previous step. The resulting polynomial is then subtracted from the original image (Image-0), pixel-by-pixel, to arrive at the globally treated image (Image-2). This essentially removes the slow varying background (1) and centers the residual background (2) about zero. By using a cubic-spline interpolation instead of a simple averaging method for the coarse graining, we can utilize the entire image including the margins and thus improve the quality of this step.

The line profiles along the rows and columns of Image-2 (obtained after the above polynomial global treatment) indicate that the remaining background is well modeled locally by, for example, 5th-order polynomials. Thus, we next partition the image into smaller blocks (typically 2 to 5 mm on a side) and within each partition least-square fit a one-dimensional 5th order polynomial to each column and/or row in the block. However, pixels from the microarray spots and other artifacts erroneously affect the fit; as a result, they need to be excluded from the fit. We have employed three methods to this end: (A) for high signal-to-noise spots, a crude global threshold may suffice. In this case, we compute the median (M-2) and the median absolute deviation (MAD-2), and use M-2 $\pm$ 3×MAD-2 to obtain a binary mask for exclusion of the microarray spots and other artifacts. Unfortunately, this does not always work well; (B) alternatively, we use a binary mask from global thresholding the differential reflectance image ($\delta R_p / R_p + \delta R_s / R_s$) of the dry microarray (before washing) to exclude these pixels. This data is readily available, but it less convenient than other methods because it requires an extra registered image; (C) in practice, it is convenient to use Image-2 and the following strategy. The signals from microarray spots of Image-2 typically have the same sign (i.e. all spots are positive relative to local background) and the spot diameters are no more than half of the center-to-center spot spacing. A grayscale morphological top hat transformation[5] can be applied to it as follows. For every pixel, we replace the value by the minimum of all pixels within a square that is centered at the pixel in question and with a side width a little larger than the spot diameter; afterward we replace the value of a pixel with the maximum of all pixels again within the same sized square centered at the pixel of interest. This procedure removes the microarray spots and other small features (e.g. dirt and small bubbles) from Image-2 and replaces them with values close to the nearby background. The resulting image (Image-3) contains the background of length scales down to twice the size of the square. We subtract Image-3 from Image-2 to eliminate the background. We then find the median (M-4) and the median absolute deviation (MAD-4) of the resulting image (Image-4) to obtain a binary mask (thresholds set at MAD-4 ± 3×MAD-4). The mask is used to exclude the microarray spots and artifacts and enables us to perform within each partition the least-square fit to a one-dimensional 5th order polynomial for each column and/or row in the block. By

subtracting the polynomial fit from Image-2 for each partition, we arrive at the final background-corrected image (Image-5). This method of automatically generating a mask from the image itself with the top hat transformation was applied to all images acquired for this study.

Spot Detection

After the locations of spots have been determined and the background has been subtracted, it remains to compute the "endpoint signal" for each spot and whether the signal suggests marking the spot "hit", "no reaction", or some other appropriate classification. This means we need to segment spot pixels from the substrate pixels as in previous steps, but do a better job of segmenting artifact pixels from spot pixels. We note that, after applying the above background subtraction procedure, most spots can be successfully segmented from the background by globally applying thresholds equal to image median ± three median deviations. In general, spot signals range from the detection limit (i.e. the standard deviation of the noise in the unprinted region of the glass surface) up to the detector saturation level. In our microarray images, the spot diameters are no more than half the center-to-center spot spacing and we generally image a wide margin around the microarray edge to improve the background correction. Thus, spot pixels comprise at most ~ 20% of the image pixels. In the histogram of signals from all pixels, the signals from the background pixels form a Gaussian peak with zero mean and the signals from the spot pixels are essentially outliers (with the exception of spots near the limit of detection). The use of the median and the median absolute deviation allows the center and dispersion of the background signal distribution to be accurately estimated despite the variable, large outliers (i.e. spot and artifact pixels). To reduce the number of false positives while keeping most weak spots, we apply an improved segmentation procedure based upon local thresholding as follows.

We first apply a noise-reducing filter to the image, such as a 3×3 Gaussian convolution mask or a 3×3 median filter. The filters reduce false positives from the stochastic noise and small punctuate artifacts (the latter are suppressed particularly well by the median filter), and the blurring of the spot edges due to filtering has little impact on spot pixel segmentation. We then use the target

readout grid to partition the microarray into rectangular boxes, each (potentially) containing a spot and its surrounding background. Since the spot pixels comprise no more than 20% of the pixels within each partition, we computed for each partition the upper and lower thresholds equal to the partition median (M_p) ± three median absolute deviations ($3\times MAD_p$). Pixels between the thresholds are considered background pixels while pixels outside the thresholds are considered *potential* spot pixels. As an option, if many spot pixels are nearby but disconnected, morphological closing can be applied to connect them. Likewise, morphological opening can be used to eliminate isolated single pixels. We next go through each partition and keep only the largest connected "binary region" (the smaller binary regions are likely to come from noise or artifacts). We then go through the binary regions and keep only those with an average radius greater than a specified threshold (a good value can be independently measured from the original dry target image of the microarray). Finally, we eliminate those remaining binary regions that lie too close to the partition boundaries (because genuine spots should be closer to the center of the partitions). If a partition has a surviving binary region, then we flag the target or the spot in the partition as a "hit candidate". The binary region is used as the mask to determine the spot pixel and background pixel statistics of each partition in the unfiltered but background corrected image. Thus, we now have a background corrected image, a target readout grid, a spot mask for segmenting out the spot pixels, and spot signals, which can be used to create useful rules for scoring "hits". For instance, we often print replicate spots of a particular target in adjacent microarray addresses. We might score a particular target as a "hit" if a majority of the adjacent replicate spots were flagged as "hit candidates" and the median of the spot signals is within acceptable thresholds.

Implementation of Global Curve Fitting

We developed a global curve fitting procedure to extract kinetic parameters of the binding reaction model from ~10,000 binding curve sets in an efficient and automated manner. *Our goal is to match the throughput of the data analysis to the throughput of the binding curve acquisition.* After real-time data is collected, the data acquisition software compensates the raw signals, zeroes the

baselines, records the probe concentration, and records the times where association and dissociation measurements begin. Additionally, the software records instrumental noises from the baselines, endpoint signals near the completion of the association and dissociation phases, and the corresponding signal-to-noise ratios (endpoint signals divided by baseline noise). After acquiring binding curves for all probe concentrations of interest, we select the binding data files to be fit, a binding model, and a signal-to-noise threshold to determine which curve sets should be fit. The rest of the process is carried out automatically. First, binding curves from the same microarray spots (but typically different probe concentrations) are collected into sets. If the median endpoint signal-to-noise ratio of the curve set exceeds a user-set threshold, then the curve set will be fit to the binding model. We use the Levenberg-Marquardt algorithm[6] to find reaction model parameters that minimize the sum of square errors (SSE) between the model and *all* the curves in the set simultaneously (global curve fitting). We observe that the instrumental noise is independent of endpoint signals; as a result, we weight all data points in all curves equally in the global fit. For the one-to-one Langmuir binding model used in this study (Eq. (2a) and Eq. (2b)), common values of k_{on} and k_{off} are applied to all curves in a given set (global fit parameters), while γN_0 is allowed to vary for each curve (local fit parameter); the probe concentrations C and dissociation starting times t_0 were recorded for each curve at the time of data acquisition. We also restrict k_{on} and k_{off} to positive values. The association and dissociation portions of the binding curves are fit simultaneously. Initial guesses for the fit parameters are obtained from a heuristic piecewise linear fit of the curves. Separate linear fits of the association and dissociation measurements converge reliably and give order of magnitude estimates of the rate constants k_{on} and k_{off} ; γN_0 is also estimated from these fits, or alternatively, from the association-phase endpoint signal. This initialization method allows the iterative Levenberg-Marquardt algorithm to proceed without human input and independent of the units of measurement (scaling) of the time and OI-RD values. The Levenberg-Marquardt algorithm iterates until the *change* in the sum of square errors falls below a threshold. To make the termination threshold independent of the signal scale, we set it equal to a constant ($\sim 1\times10^{-6}$) times the maximum curve endpoint signal in the set. To increase the likelihood

that the output parameter values give a global rather than a local minimum of the sum of square errors, the heuristic initial values are randomly perturbed and input to the Levenberg-Marquardt algorithm; the output parameter set with the smallest sum of square errors is retained. The perturbations are drawn from zero-mean Gaussian distributions with standard deviations equal to the heuristic parameter value. In the present study, this was performed ten times per set of binding curves. More trials are rarely needed with the Langmuir model, *keeping the time needed to fit ~ 10,000 curve sets to ~ 1 hour* using our current computer software and hardware. Analysis time can be further reduced by fitting batches of curve sets in parallel using modern multi-core computer processors. Finally, we observe that the instrumental noise in the baseline is distributed normally, allowing us to estimate the uncertainties of the output fit parameters using the diagonal elements of the Levenberg-Marquardt output covariance matrix and the final root mean square error of the fit.

Numerical simulations of Langmuir kinetics (**Figure S-10** and **Table S-2** for a reaction with significant dissociation and **Figure S-11** and **Table S-3** for a reaction with little dissociation) with Gaussian noise and random values of γN_0 (to simulate the variability of microarray printing) demonstrates that our global curve fitting procedure successfully extracts meaningful values for k_{on}, k_{off}, and γN_0 even for low signal-to-noise ratio (< 5) data. After curve fitting, the output value for the off-rate, k_{off}, is further assessed as described below.

FIGURE S-10

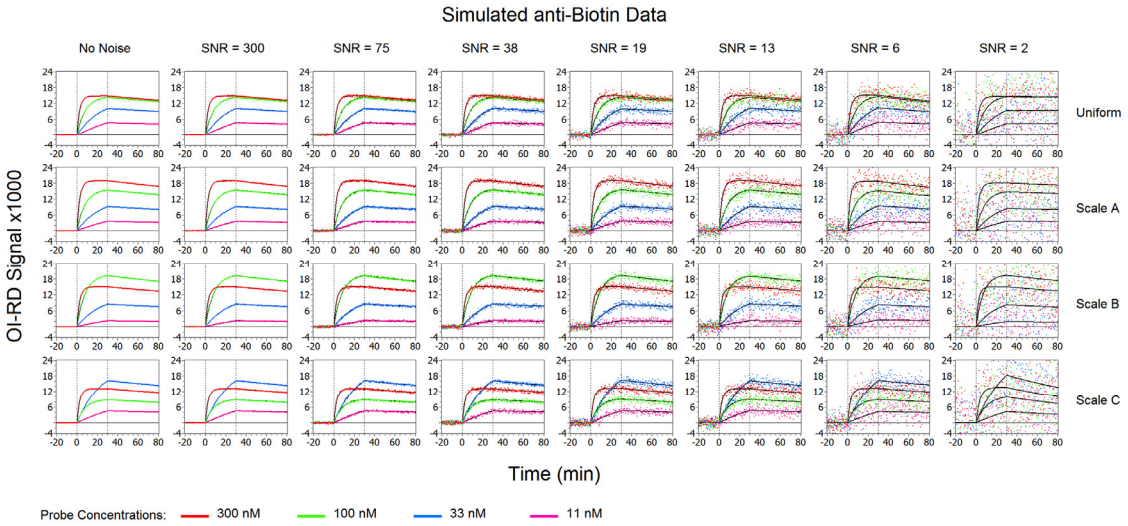

Simulated binding curves mimicking experimental data for mouse IgG reaction with biotin targets. The time interval between successive points is 25 s. The kinetic parameters are $k_{on} = 2 \times 10^{-5}$ $(nM \cdot s)^{-1}$ and $k_{off} = 4 \times 10^{-5}$ s^{-1}. Curves were calculated for probe concentrations at 300 nM (red curves), 100 nM (green curves), 33 nM (blue curves), and 11 nM (violet curves). For the "Uniform Scale" panel, a scale factor of $\gamma N_0 = 1.5 \times 10^{-2}$ was assumed. For the "Scale A", "Scale B", and "Scale C" panels, random values of γN_0 where drawn from a uniform distribution on the interval $[5 \times 10^{-3}, 2.5 \times 10^{-2}]$ for each probe concentration. From highest to lowest probe concentration, the values used for "Scale A" are 1.92×10^{-2}, 1.62×10^{-2}, 1.36×10^{-2} and 1.15×10^{-2}; for "Scale B", 1.52×10^{-2}, 2.02×10^{-2}, 1.26×10^{-2}, and 7.09×10^{-3}; for "Scale C", 1.33×10^{-2}, 9.20×10^{-3}, 2.41×10^{-2}, and 1.44×10^{-2}. For each set of scales, curves were calculated with additive Gaussian noise with means of zero and standard deviations of 5×10^{-5}, 2×10^{-4}, 4×10^{-4}, 8×10^{-4}, 1.2×10^{-3}, 2.4×10^{-3}, and 2.4×10^{-3}. The black curves show the results of globally fitting the four simulated binding curves wherein k_{on} and k_{off} are shared fit parameters, but γ is allowed to vary from curve to curve.

TABLE S-2: Global fitting parameters obtained from simulated binding curves (**Figure S-10**). For each scale and noise level, the set of four simulated binding curves was globally fit wherein k_{on} and k_{off} were shared fit parameters, but γN_0 was allowed to vary from curve to curve. The signal-to-noise ratio is calculated using SNR = 1.5×10^{-2}/Noise, where 1.5×10^{-2} is the mean value of γN_0. Noise is the standard deviation of the zero-mean additive Gaussian noise in the simulated data. In this case both the fitted dissociation rate constants and the association rate constants are not dominated by the noise even at SNR = 6 or below.

Scale	Noise	SNR	k_{on} $(nM \cdot s)^{-1}$	k_{off} (s^{-1})	K_d (nM)
Uniform	0	∞	2×10^{-5}	4×10^{-5}	2
	5×10^{-5}	300	$1.996 \pm 0.004 \times 10^{-5}$	$4.00 \pm 0.01 \times 10^{-5}$	2.004 ± 0.008
	2×10^{-4}	75	$1.97 \pm 0.01 \times 10^{-5}$	$3.99 \pm 0.06 \times 10^{-5}$	2.02 ± 0.03
	4×10^{-4}	38	$1.98 \pm 0.03 \times 10^{-5}$	$4.2 \pm 0.1 \times 10^{-5}$	2.11 ± 0.07
	8×10^{-4}	19	$2.05 \pm 0.06 \times 10^{-5}$	$3.5 \pm 0.2 \times 10^{-5}$	1.7 ± 0.1
	1.2×10^{-3}	13	$1.99 \pm 0.09 \times 10^{-5}$	$3.9 \pm 0.4 \times 10^{-5}$	2.0 ± 0.2
	2.4×10^{-3}	6	$1.9 \pm 0.2 \times 10^{-5}$	$5.3 \pm 0.7 \times 10^{-5}$	2.7 ± 0.4
	7.5×10^{-3}	2	$1.9 \pm 0.5 \times 10^{-5}$	$< 4 \times 10^{-5}$	< 2.1
A	0	∞	2×10^{-5}	4×10^{-5}	2
	5×10^{-5}	300	$2.004 \pm 0.003 \times 10^{-5}$	$4.00 \pm 0.01 \times 10^{-5}$	1.997 ± 0.007
	2×10^{-4}	75	$2.00 \pm 0.01 \times 10^{-5}$	$3.97 \pm 0.05 \times 10^{-5}$	1.99 ± 0.03
	4×10^{-4}	38	$1.99 \pm 0.02 \times 10^{-5}$	$4.0 \pm 0.1 \times 10^{-5}$	2.02 ± 0.06
	8×10^{-4}	19	$1.91 \pm 0.05 \times 10^{-5}$	$4.1 \pm 0.2 \times 10^{-5}$	2.1 ± 0.1
	1.2×10^{-3}	13	$1.92 \pm 0.07 \times 10^{-5}$	$3.8 \pm 0.3 \times 10^{-5}$	2.0 ± 0.2
	2.4×10^{-3}	6	$2.2 \pm 0.2 \times 10^{-5}$	$4.4 \pm 0.6 \times 10^{-5}$	2.0 ± 0.3
	7.5×10^{-3}	2	$2.0 \pm 0.5 \times 10^{-5}$	$< 3.1 \times 10^{-5}$	< 1.6
B	0	∞	2×10^{-5}	4×10^{-5}	2
	5×10^{-5}	300	$2.006 \pm 0.003 \times 10^{-5}$	$3.98 \pm 0.01 \times 10^{-5}$	1.982 ± 0.007
	2×10^{-4}	75	$2.02 \pm 0.01 \times 10^{-5}$	$4.02 \pm 0.06 \times 10^{-5}$	1.98 ± 0.03
	4×10^{-4}	38	$1.99 \pm 0.02 \times 10^{-5}$	$3.9 \pm 0.1 \times 10^{-5}$	1.95 ± 0.06
	8×10^{-4}	19	$1.93 \pm 0.05 \times 10^{-5}$	$4.3 \pm 0.2 \times 10^{-5}$	2.2 ± 0.1
	1.2×10^{-3}	13	$2.17 \pm 0.08 \times 10^{-5}$	$3.5 \pm 0.3 \times 10^{-5}$	1.6 ± 0.2
	2.4×10^{-3}	6	$2.1 \pm 0.2 \times 10^{-5}$	$3.3 \pm 0.6 \times 10^{-5}$	1.6 ± 0.3
	7.5×10^{-3}	2	$2.3 \pm 0.5 \times 10^{-5}$	$4 \pm 2 \times 10^{-5}$	1.6 ± 0.9
C	0	∞	2×10^{-5}	4×10^{-5}	2
	5×10^{-5}	300	$1.999 \pm 0.004 \times 10^{-5}$	$4.02 \pm 0.02 \times 10^{-5}$	2.011 ± 0.009
	2×10^{-4}	75	$2.03 \pm 0.02 \times 10^{-5}$	$4.03 \pm 0.06 \times 10^{-5}$	1.98 ± 0.04
	4×10^{-4}	38	$2.06 \pm 0.04 \times 10^{-5}$	$3.7 \pm 0.1 \times 10^{-5}$	1.79 ± 0.07
	8×10^{-4}	19	$1.93 \pm 0.07 \times 10^{-5}$	$4.6 \pm 0.2 \times 10^{-5}$	2.4 ± 0.2
	1.2×10^{-3}	13	$2.0 \pm 0.1 \times 10^{-5}$	$4.1 \pm 0.4 \times 10^{-5}$	2.0 ± 0.2
	2.4×10^{-3}	6	$1.9 \pm 0.2 \times 10^{-5}$	$3.7 \pm 0.7 \times 10^{-5}$	1.9 ± 0.4
	7.5×10^{-3}	2	$1.5 \pm 0.5 \times 10^{-5}$	$1.0 \pm 0.2 \times 10^{-5}$	7 ± 3

FIGURE S-11

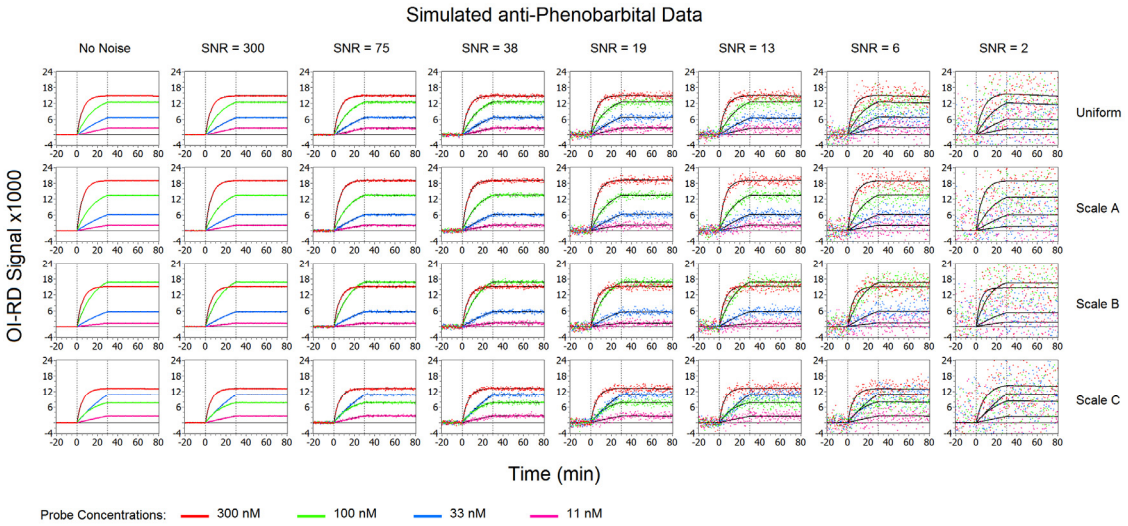

Simulated binding curves mimicking the anti-phenobarbital data. The kinetic parameters used are $k_{on} = 1 \times 10^{-5}$ $(nM \cdot s)^{-1}$ and $k_{off} = 8 \times 10^{-7}$ s^{-1}. All other simulation parameters are the same as for **Figure S-10**.

TABLE S-3: Global fitting parameters obtained from the simulated anti-phenobarbital binding curves in Fig. S-11. For each scale and noise level, the four simulated binding curves were globally fit wherein k_{on} and k_{off}, were shared fit parameters, but γN_0 was allowed to vary from curve to curve. The signal-to-noise ratio is calculated using SNR = 1.5×10^{-2}/Noise, where 1.5×10^{-2} is the mean value of γN_0. Noise is the standard deviation of the zero-mean additive Gaussian noise in the simulated data. It is clear that in this case study, the fitted dissociation rate constants are dominated by the noise even with SNR < 300, while the fitted association rate constants are not.

Scale	Noise	SNR	k_{on} $(nM \cdot s)^{-1}$	k_{off} (s^{-1})	K_d (nM)
Uniform	0	∞	1×10^{-5}	8×10^{-7}	0.08
	5×10^{-5}	300	$1.003 \pm 0.002 \times 10^{-5}$	$5 \pm 2 \times 10^{-7}$	0.05 ± 0.02
	2×10^{-4}	75	$9.92 \pm 0.08 \times 10^{-6}$	$< 1.0 \times 10^{-6}$	< 0.11
	4×10^{-4}	38	$9.8 \pm 0.2 \times 10^{-6}$	$3 \pm 1 \times 10^{-6}$	0.3 ± 0.1
	8×10^{-4}	19	$1.06 \pm 0.03 \times 10^{-5}$	$< 4.4 \times 10^{-6}$	< 0.42
	1.2×10^{-3}	13	$9.2 \pm 0.4 \times 10^{-6}$	$< 6.0 \times 10^{-6}$	< 0.65
	2.4×10^{-3}	6	$1.0 \pm 0.1 \times 10^{-5}$	$< 1.4 \times 10^{-5}$	< 1.4
	7.5×10^{-3}	2	$8 \pm 2 \times 10^{-6}$	$< 3.9 \times 10^{-5}$	< 5
A	0	∞	1×10^{-5}	8×10^{-7}	0.08
	5×10^{-5}	300	$9.99 \pm 0.02 \times 10^{-6}$	$9 \pm 1 \times 10^{-7}$	0.09 ± 0.01
	2×10^{-4}	75	$1.000 \pm 0.007 \times 10^{-5}$	$1.5 \pm 0.6 \times 10^{-6}$	0.15 ± 0.06
	4×10^{-4}	38	$1.00 \pm 0.01 \times 10^{-5}$	$< 1.7 \times 10^{-6}$	< 0.17
	8×10^{-4}	19	$9.8 \pm 0.3 \times 10^{-6}$	$< 3.4 \times 10^{-6}$	< 0.35
	1.2×10^{-3}	13	$1.02 \pm 0.04 \times 10^{-5}$	$< 4.8 \times 10^{-6}$	< 0.47
	2.4×10^{-3}	6	$8.9 \pm 0.7 \times 10^{-6}$	$< 1.0 \times 10^{-5}$	< 1.2
	7.5×10^{-3}	2	$9 \pm 2 \times 10^{-6}$	$< 3.4 \times 10^{-5}$	< 3.8
B	0	∞	1×10^{-5}	8×10^{-7}	0.08
	5×10^{-5}	300	$9.96 \pm 0.02 \times 10^{-6}$	$1.0 \pm 0.1 \times 10^{-6}$	0.10 ± 0.01
	2×10^{-4}	75	$9.91 \pm 0.07 \times 10^{-6}$	$1.9 \pm 0.6 \times 10^{-6}$	0.19 ± 0.06
	4×10^{-4}	38	$1.00 \pm 0.02 \times 10^{-5}$	$< 2.0 \times 10^{-6}$	< 0.20
	8×10^{-4}	19	$1.02 \pm 0.03 \times 10^{-5}$	$< 4.0 \times 10^{-6}$	< 0.40
	1.2×10^{-3}	13	$1.04 \pm 0.05 \times 10^{-5}$	$< 6.0 \times 10^{-6}$	< 0.58
	2.4×10^{-3}	6	$1.04 \pm 0.09 \times 10^{-5}$	$< 1.1 \times 10^{-5}$	< 1.1
	7.5×10^{-3}	2	$1.4 \pm 0.4 \times 10^{-6}$	$< 3.8 \times 10^{-5}$	< 2.8
C	0	∞	1×10^{-5}	8×10^{-7}	0.08
	5×10^{-5}	300	$9.98 \pm 0.02 \times 10^{-6}$	$9 \pm 2 \times 10^{-7}$	0.10 ± 0.02
	2×10^{-4}	75	$9.98 \pm 0.09 \times 10^{-6}$	$< 1.2 \times 10^{-6}$	< 0.12
	4×10^{-4}	38	$9.7 \pm 0.2 \times 10^{-6}$	$< 2.5 \times 10^{-6}$	< 0.26
	8×10^{-4}	19	$9.7 \pm 0.4 \times 10^{-6}$	$< 4.9 \times 10^{-6}$	< 0.51
	1.2×10^{-3}	13	$1.09 \pm 0.06 \times 10^{-5}$	$< 7.2 \times 10^{-6}$	< 0.66
	2.4×10^{-3}	6	$1.0 \pm 0.1 \times 10^{-5}$	$< 1.5 \times 10^{-5}$	< 1.5
	7.5×10^{-3}	2	$6 \pm 2 \times 10^{-6}$	$< 4.0 \times 10^{-5}$	< 6.3

Estimation of an Upper Bound for the Dissociation Rates of High-Affinity Binders

A most important use of kinetic rate constants obtained from real-time binding curves is the determination of the equilibrium association constant K_a, given by $K_a = k_{on}/k_{off}$. K_a is the measure of the binding affinity between a probe and a target. Often the difference in K_a comes mainly from the difference in k_{off} rather than k_{on}. That is, high-affinity binding reactions have low values of k_{off} and vice versa.

For reactions with equilibrium association constants K_a larger than 10 nM^{-1}, (i.e., K_d less than 0.1 nM), we only report the 68% confidence *upper bounds* (the Langmuir kinetic parameters must be nonnegative). The reason is as follows: When the change in optical signal due to probe dissociation over the observation time of dissociation phase (60 minutes in this experiment) is less than the background noise in the signal, the dissociation portion of the binding curve is essentially flat and as a result k_{off} deduced from the curve-fitting is less than its standard deviation (determined by the noise from the curve-fitting). In this case, it is only sensible to use the standard deviation of k_{off} to set an upper bound for k_{off}. We next derive a simple algorithm for finding such an upper bound for the dissociation rate (and in turn the lower bound for the equilibrium association constants K_a). It is a function of the signal-to-noise ratio, the time duration of dissociation phase, and the data-sampling rate. This notion of establishing an upper bound for k_{off} and in turn, an upper bound for K_a from experimental data applies to analysis of real-time binding curves obtained by other label-free techniques.

For binding curve measurements, an observation time up to an hour is typical. In comparison, the time for 10% of the bound probes to dissociate from the targets is $0.1/k_{off}$. For high-affinity reactions, $0.1/k_{off}$ can be hours or even days. This poses a significant challenge for high-throughput binding curve measurement as the dissociation reaction observation time will need to be much less than $0.1/k_{off}$. In these cases, the dissociation portion of the binding curves will be more or less flat. Because the noise in the dissociation data is inevitable, the extraction of k_{off} can be dominated by the noise, namely, the uncertainty of k_{off}, rather than the fitting parameter. If the signal-to-noise ratio is too low, k_{off} from the fitting routine may vary by orders of magnitude, depending on the fitting initial

conditions and the termination threshold. Furthermore, the uncertainty in the fitted k_{off} may be larger than the fitted k_{off} itself, indicating that the latter is meaningless and the former sets a meaningful upper bound for k_{off}. We show that an *upper bound* for k_{off} is given by

$$k_{off,\max} = \frac{2\sqrt{3}\cdot\sigma}{\Delta\delta(t_0)\cdot T\sqrt{N}}, \tag{S-3}$$

where T is the observation time for the dissociation phase of the binding reaction, N is the number of evenly spaced measurement points of the dissociation curve, $\Delta\delta(t_0)$ is the observed OI-RD signal at $t = t_0$ (the beginning of the dissociation phase), and σ is the standard deviation of the noise in the OI-RD signal. We note that T, N, and $\Delta\delta(t_0)$ are readily available from the measurements. The instrumental noise σ can be obtained from a reference baseline acquired before the association reaction begins. This relationship is also useful for designing dissociation experiments to achieve a particular upper bound, as discussed later.

In this study, we measured ~ 10,000 antibody-antigen interactions with the dissociation curves mostly flat during one-hour observation of the dissociation phase. Let the parameter values from the global curve be $k_{on,\mathrm{fit}}$ and $k_{off,\mathrm{fit}}$ and the respective uncertainties be σ_{on} and σ_{off}. In a global curve fitting, these values are common to all the curves in the fitted set. The corresponding equilibrium dissociation constant is calculated as $K_{d,\mathrm{fit}} = k_{off,\mathrm{fit}}/k_{on,\mathrm{fit}}$ with the uncertainty given by $\sigma_d = K_{d,\mathrm{fit}}\sqrt{\left(\sigma_{off}/k_{off,\mathrm{fit}}\right)^2 + \left(\sigma_{on}/k_{on,\mathrm{fit}}\right)^2}$. We assume that the fit adequately describes the data such that the root mean square error (RMSE) evaluated using the fitting parameters is approximately equal to the instrumental noise, $\sigma \approx \mathrm{RMSE}$, and thus $k_{on} = k_{on,\mathrm{fit}} \pm \sigma_{on}$ is a reasonable estimate of the association rate constant. If there is a significant decay beyond the noise during the dissociation phase, then $k_{off} = k_{off,\mathrm{fit}} \pm \sigma_{off}$ is a good estimate for the dissociation rate; otherwise, only an upper bound can be established. To distinguish between these two cases, we calculate values of $k_{off,\max}^{(i)}$ using Eq. (S-3) for each curve $i = 1,\ldots,M$ (where M is the number of binding curves in a set used in the global fit). In these calculations, we approximate σ using the RMSE calculated for the curve

under consideration. For each curve we then determine a value of $k_{off}^{(i)}$ such that $k_{off}^{(i)} = k_{off,\max}^{(i)}$ if $k_{off,\text{fit}} < k_{off,\max}^{(i)}$, otherwise $k_{off}^{(i)} = k_{off,\text{fit}}$. We assign $k_{off,\text{best}} = \min\left\{k_{off}^{(i)}\right\}_{i=1}^{M}$ and $K_{d,\text{best}} = k_{off,\text{best}} / k_{on,\text{fit}}$. If $k_{off,\text{best}} = k_{off,\text{fit}}$, we report $k_{off} = k_{off,\text{best}} \pm \sigma_{off}$ and $K_d = K_{d,\text{best}} \pm \sigma_d$; otherwise we report $k_{off} < k_{off,\text{best}}$ and $K_d < K_{d,\text{best}}$.

We now consider some limiting cases. If all binding curves exhibit significant decay beyond the noise level, we naturally have $k_{off}^{(i)} = k_{off,\text{fit}}$ for all the curves. This is because $k_{off,\max}^{(i)}$ is calculated from the fit RMSE for each curve and thus $k_{off,\text{fit}} > k_{off,\max}^{(i)}$. If all the binding curves in the dissociation phase are essentially flat, we arrive at $k_{off,\text{best}} = \min\left\{k_{off,\max}^{(i)}\right\}_{i=1}^{M}$. Since the values of $k_{off,\max}^{(i)}$ are upper bounds for the true value of k_{off}, it is sensible to report the smallest of all. In this situation, the value for $k_{off,\text{best}}$ is determined by the curve with the highest signal-to-noise ratio ($\text{SNR} \sim \Delta\delta(t_0)/\sigma$) since the other parameters (T and N) are usually the same from curve to curve. In general, some $k_{off}^{(i)}$ are fit values and some are upper bounds. Clearly, if the minimum value of a mixed set is a fit value, then this fit value is self-consistent with upper bound values present in the set and therefore our prescription gives a sensible answer. If the minimum value of a mixed set is an upper bound, the interpretation needs caution. In this case, the data should be examined to see if there is a curve that is poorly described by the fit model due to experimental artifacts. The questionable curves should be corrected or eliminated and the fit and the subsequent analysis should be reapplied. Lastly, we note that our prescription provides robust upper bounds even in the presence of uncorrected experimental artifacts in the data. This is true because the RMSE value used in the prescription will generally be larger than the true value of the stochastic instrumental noise σ due to the artifacts. Numerical demonstrations of the validity of the prescription are provided with simulated Langmuir binding data with Gaussian noise in **Figure S-10, Figure S-11, Table S-2,** and **Table S-3.**

Derivation of the Upper Bound $k_{off,\max}$ for Dissociation Rate Constant

Here we derive Eq. (S-3) presented in the previous section. We also discuss the application of this equation to designing dissociation experiments. According to Eq. (2b), the OI-RD signal during the dissociation reaction ($t > t_0$) is given by

$$\Delta\delta(t) = \Delta\delta(t_0)e^{-k_{off}(t-t_0)} \tag{S-4}$$

where

$$\Delta\delta(t_0) = \gamma N_0 \cdot \frac{k_{on}C}{k_{on}C + k_{off}}\left(1 - e^{-(k_{on}C+k_{off})t_0}\right). \tag{S-5}$$

We now assume that $t - t_0 << 1/k_{off}$ during the entire length of the dissociation phase. The hallmark of this condition is that the observed decay is linear. Thus Eq. (S-4) can be approximated as $\Delta\delta(t) \approx a + b(t - t_0)$, where $a = \Delta\delta(t_0)$ and $b = -\Delta\delta(t_0)\cdot k_{off}$. The dissociation rate $k_{off} = -b/a$ can be obtained from a linear least squares fit of the dissociation data[6]. The linear least squares fit also yields estimates for the slope uncertainty $\sigma\{b\}$ and intercept uncertainty $\sigma\{a\}$, giving the uncertainty in the dissociation rate as $\sigma\{k_{off}\} = k_{off}\sqrt{(\sigma\{a\}/a)^2 + (\sigma\{b\}/b)^2}$, by propagation of errors. Let N be the number of measurements (readouts) made during the dissociation reaction, Δt be the time between successive measurements (readouts), and $T = (N-1)\Delta t$ be the total duration of observation. Furthermore, let $\sigma = \sigma\{\Delta\delta\}$ be the uncertainty in each OI-RD observation (i.e. the instrumental noise). For large values of N (i.e. $N > \sim 20$), the standard equations for the uncertainties (see, for example, Eq. 6.23 in Reference 6) reduce to $\sigma\{b\} \approx (2\sqrt{3}\sigma)/(T\sqrt{N})$ and $\sigma\{a\} \approx (2\sigma)/\sqrt{N}$. Therefore the uncertainty in the dissociation rate constant is

$$\sigma\{k_{off}\} \approx \frac{2\sigma}{\Delta\delta(t_0)\sqrt{N}}\sqrt{3/T^2 + k_{off}^2} \approx \frac{2\sqrt{3}\cdot\sigma}{\Delta\delta(t_0)\cdot T\sqrt{N}}. \tag{S-6}$$

If $k_{off} = -b/a < \sigma\{k_{off}\}$, only $\sigma\{k_{off}\}$ is meaningful and sets an *upper bound* for the true value of k_{off} as

$$k_{off,\max} = \frac{2\sqrt{3}\cdot\sigma}{\Delta\delta(t_0)\cdot T\sqrt{N}}. \tag{S-7}$$

It is notable that all the parameters in this equation are obtainable from the data. If $k_{on}C >> k_{off}$, $\Delta\delta(t_0) \approx \gamma N_0 \cdot \left(1 - e^{-k_{on}Ct_0}\right)$ in Eq. (S-7). Since γN_0 is the OI-RD signal at the equilibrium, a useful definition of the signal-to-noise ratio of the data is SNR = $\gamma N_0/\sigma$. In this case, Eq. (S-7) can be rewritten as

$$k_{off,\max} \approx \frac{2\sqrt{3}\cdot\sqrt{\Delta t}}{T^{3/2}\cdot \mathrm{SNR}\cdot\left(1 - e^{-k_{on}Ct_0}\right)}. \tag{S-8}$$

This form is useful for designing dissociation experiments. A smaller value of $k_{off,\max}$ gives a tighter bound on k_{off} and therefore Eq. S-8 makes it clear that short sampling periods, long observation times, and high signal-to-noise ratios are desirable, as intuitively expected. The smallest achievable sampling period Δt is limited by the scanning hardware and the number of microarray spots to be read out; thus Δt is not very convenient for tuning $k_{off,\max}$. It should be pointed out that smoothing the data, such as by convolution or median filters, to increase the apparent SNR does not reduce $k_{off,\max}$. This is because smoothing operations also increase the effective value of Δt by a factor of the half-width of the smoothing window, canceling out the gain in SNR (which scales roughly as the square root of the window half-width). Therefore tuning $k_{off,\max}$ through SNR must come through boosting the signal, such as by increasing the surface density of binding sites N_0. Additionally, one can boost the signal by choosing probe concentration C or association reaction duration t_0 to bring the association signal near equilibrium ($e^{-k_{on}Ct_0} \sim 0$). Lastly, one can choose to observe the dissociation reaction for a longer time. Since Δt is a constant for all practical purposes, Eq. (S-8) shows that $k_{off,\max} \propto T^{-3/2}$. For example, a 100-fold decrease in $k_{off,\max}$ requires a 20-fold increase in observation time.

SUPPLEMENT REFERENCES

1. Landry, J. P., Zhu, X. D. & Gregg, J. P. Label-free detection of microarrays of biomolecules by oblique-incidence reflectivity difference microscopy. *Optics Letters* **29**, 581-3 (2004).

2. Fei, Y. Y. et al. A novel high-throughput scanning microscope for label-free detection of protein and small-molecule chemical microarrays. *Review of Scientific Instruments* **79**, 013708-7 (2008).

3. Zhu, X. et al. Oblique-incidence reflectivity difference microscope for label-free high-throughput detection of biochemical reactions in a microarray format. *Applied Optics* **46**, 1890-1895 (2007).

4. Landry, J. P., Sun, Y. S., Lam, K. S. & Zhu, X. D. High-Throughput Endpoint and Real-Time Detection of Biochemical Reactions in Microarrays Using Label-Free Oblique-Incidence Reflectivity Difference Microscopes. *Conference on Lasers and Electro-Optics/Quantum Electronics and Laser Science Conference and Photonic Applications Systems Technologies*, CTuV7 (2007).

5. Gonzalez, R. C. & Woods, R. E. *Digital image processing* (Prentice Hall, 2002).

6. Bevington, P. R. & Robinson, D. K. *Data Reduction and Error Analysis for the Physical Sciences* (McGraw-Hill, 1992).